nature geoscience

REVIEW ARTICLE

https://doi.org/10.1038/s41561-021-00859-1

Poleward expansion of tropical cyclone latitudes in warming climates

Joshua Studholme[1]✉, Alexey V. Fedorov[1,2], Sergey K. Gulev[3], Kerry Emanuel[4] and Kevin Hodges[5]

Tropical cyclones (TCs, also known as hurricanes and typhoons) generally form at low latitudes with access to the warm waters of the tropical oceans, but far enough off the equator to allow planetary rotation to cause aggregating convection to spin up into coherent vortices. Yet, current prognostic frameworks for TC latitudes make contradictory predictions for climate change. Simulations of past warm climates, such as the Eocene and Pliocene, show that TCs can form and intensify at higher latitudes than of those during pre-industrial conditions. Observations and model projections for the twenty-first century indicate that TCs may again migrate poleward in response to anthropogenic greenhouse gas emissions, which poses profound risks to the planet's most populous regions. Previous studies largely neglected the complex processes that occur at temporal and spatial scales of individual storms as these are poorly resolved in numerical models. Here we review this mesoscale physics in the context of responses to climate warming of the Hadley circulation, jet streams and Intertropical Convergence Zone. We conclude that twenty-first century TCs will most probably occupy a broader range of latitudes than those of the past 3 million years as low-latitude genesis will be supplemented with increasing mid-latitude TC favourability, although precise estimates for future migration remain beyond current methodologies.

Tropical cyclones (TCs) start as $O(10^4)$ km^2 clusters of individual thunderstorms weakly rotating around a common axis. The transition from disaggregated convection into a coherent cyclone can occur over hours, days or weeks, as vorticity increases by two orders of magnitude to produce surface winds of over 15 m s^{-1} (Extended Fig. 1)[1,2]. Once formed, TCs generally move westward and poleward before they interact with mid-latitude westerlies and weather systems, and in some cases transition into frontal systems in the extratropics (Fig. 1). Locally, the physics of evaporation, friction, convection, entrainment, and radiation determine the vortex lifecycle[3,4]. Box 1 summarizes these core elements of TC formation, intensification and propagation—the TC lifecycle. How local physics and equator-to-pole TC distribution relate to one another has been discussed for at least a century[5] and yet fundamental disagreement about how TC latitudes depend on climate persists[6]. In this review, we synthesize recent advances and attempt to connect the heuristic view above with a well-defined physical basis for TC latitudinal distribution.

One of the central outcomes of this review is to establish the fundamental roles that convective mesoscale processes play in linking the climatological TC occurrence to large-scale atmospheric dynamics in different climates. This emergent view is novel because the lifecycle evolution of TCs, and its intrinsic mesoscale processes, have historically been overlooked in TC climate studies. Instead, the focus has been on whether or not TCs would emerge from a given climatology of wind, temperature and humidity[7] (see 'Tropical cyclogenesis as a dynamical process'). This well-established framework is underpinned by empirical 'genesis potential indices' (GPIs)—best guesses at the functional forms and coefficients for controls on TC formation that are calibrated against the observed TC distribution. Often GPIs are used in tandem with simple TC models that passively propagate cyclones through environmental winds (Box 1) neglecting their two-way interactions with the atmospheric environment (known as 'statistical downscaling')[8].

These diagnostic methods are adopted, in part, because climate simulations with general circulation models (GCMs) struggle to resolve realistic TCs[9]. A contrasting approach nests higher-resolution models within lower-resolution ones (known as 'dynamical downscaling'). Both dynamical and statistical downscaling approaches are used to enumerate how past, present and future climates produce TCs (see 'Past, present and potential latitudinal migrations'). The problem is that these contrasting approaches yield vastly different interpretations of twenty-first century climate projections[10–13], which thus establishes the necessity for a prognostic understanding of the relationship between TCs and climate[6]. In this review, we conclude that a joint consideration of the convective mesoscale processes that occur within TCs and the large-scale dynamics of the atmospheric Hadley circulation, Intertropical Convergence Zone (ITCZ) and tropospheric jet streams enables a new framework to understand the relationship of TCs to climate (see 'Linking mesoscale physics to large-scale climate dynamics'). As discussed later, these links have implications for reducing uncertainty in the projections of twenty-first century TCs.

Tropical cyclogenesis as a dynamical process

As a core methodology in modern TC–climate studies, GPIs reproduce the broad-brush characteristics of observed TC genesis, particularly at basin-averaged scales[3]. GPIs do substantially worse at reproducing the characteristics of TC genesis simulated by GCMs[9,14]. We note that, although appropriate GPI formulations should only use variables explicitly relevant to TC physics, they often use free tropospheric relative humidity rather than water vapour saturation deficit (or free tropospheric dryness relative to the boundary layer) as the moisture variable, despite the established physical relevance of the latter but not the former[15]. Although GPI variants perform equally well in reproducing TC genesis patterns of current climate, they diverge in describing future changes[15]. Moreover, the greenhouse warming response of an individual state-of-the-art GPI,

[1]Yale University, New Haven, CT, USA. [2]LOCEAN/IPSL, Sorbonne University, Paris, France. [3]Shirshov Institute of Oceanology, Moscow, Russia. [4]Massachusetts Institute of Technology, Cambridge, MA, USA. [5]University of Reading, Reading, UK. ✉e-mail: joshua.studholme@yale.edu

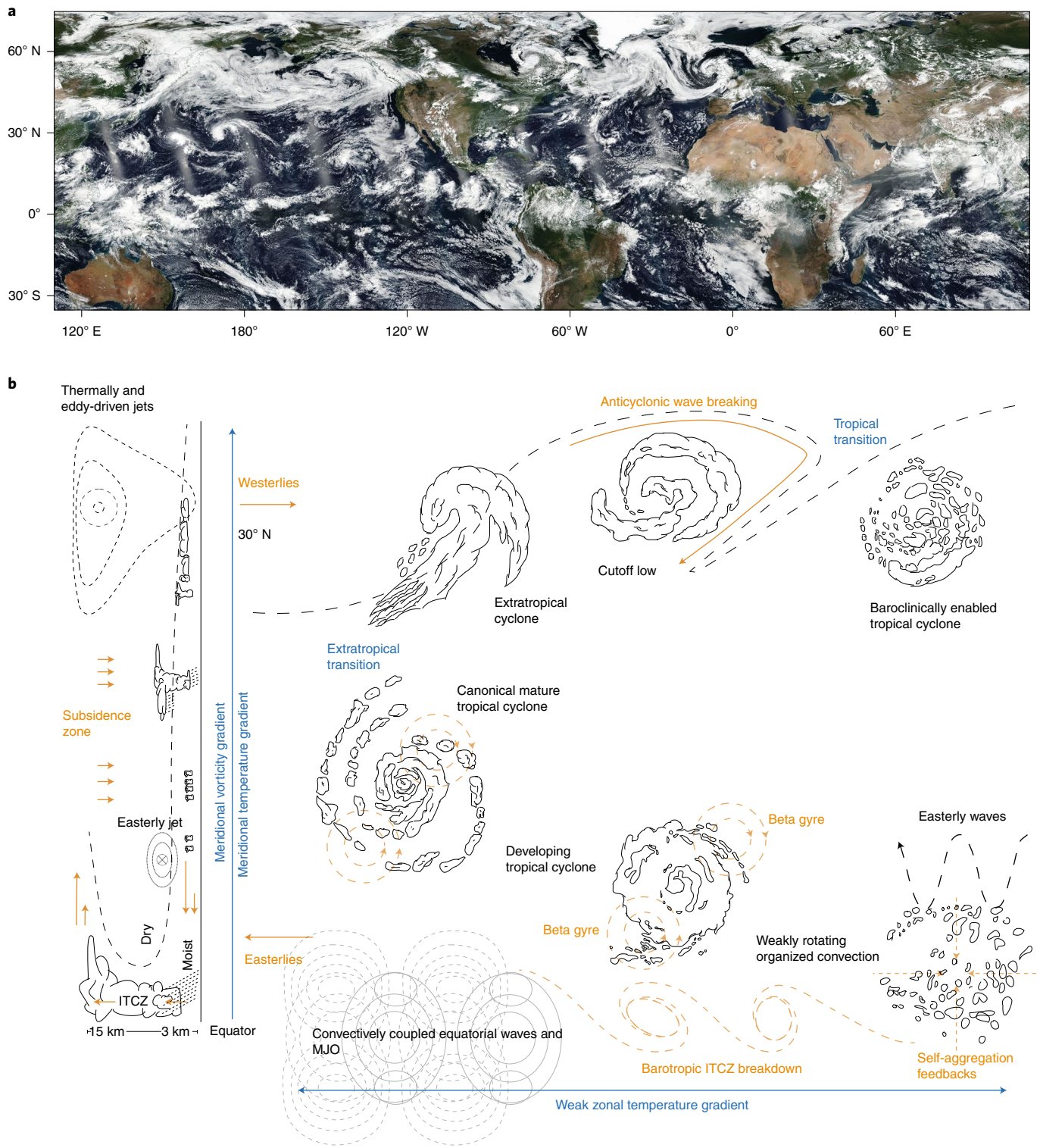

Fig. 1 | Tropical cyclogenesis in weather and climate. a, Earth's atmosphere on 22 July 2017 from NASA EOSDIS[154]. This day exhibits the most simultaneously existing TCs in the satellite record. Tropical Storms Roke (peak intensity 18 m s^{-1}), Sonca (18 m s^{-1}), Kulap (20 m s^{-1}) and Typhoon Noru (49 m s^{-1}) are seen in the western subtropical North Pacific. In the eastern North Pacific, Hurricane Fernanda (65 m s^{-1}), Tropical Storm Greg (27 m s^{-1}), Hurricane Hilary (49 m s^{-1}) and Hurricane Irwin (40 m s^{-1}) are seen at various development stages. **b**, Schematic of traditional and baroclinically enabled tropical cyclogenesis embedded into the large-scale flow and atmospheric dynamics (see Extended Data Figs. 1 and 2 for examples). The schematic style of the tropical mean circulation follows that of Bony et al.[155].

which uses the physically consistent moisture variable of saturation deficit, has been shown to change sign when the empirical coefficient for that variable is modified without degrading the fit to observations[11]. More troubling still, the statistical relationship between the time-mean environmental fields used to calculate GPIs and TC distribution is not necessarily consistent between the observations and models, and between models using different dynamical cores, resolutions and physics[16,17].

Box 1 | Elemental controls

Potential intensity. PI theory[175], the only extant analytical framework for TC's environmental dependences, states that TC strength is regulated by (1) the rate of oceanic heat extraction (mainly through evaporation), (2) frictional dissipation at the ocean surface and (3) thermodynamic efficiency, also called the Carnot efficiency (the normalized difference between ocean surface and TC outflow temperatures) (Methods). The Carnot efficiency concept from classical thermodynamics is modified in the context of TCs to incorporate additional heating due to frictional energy dissipation. An upper bound on TC wind speeds can be inferred from this framework and computed in various ways from gridded climate data. PI theory predicted three decades ago that anthropogenic warming would increase PI in warmer climates[176] and so increase the occurrence of intense TCs (as opposed to more TCs of all strengths). This expectation has now been validated in recent observational data[177].

Convective aggregations. When PI is high enough and an aggregation of high entropy air has occurred, the necessary thermodynamic conditions for TC genesis are satisfied[4]. High entropy, or alternatively high moist static energy (MSE) (Methods), follows from warm and moist air columns that are established by surface evaporation and sensible heat transfer, radiative fluxes and horizontal advection. These aggregations may originate from a wide variety of synoptic and mesoscale disturbances with embedded convective systems: easterly waves, barotropic breakdown of the ITCZ, convectively coupled equatorial waves (CCEW), the Madden–Julian Oscillation (MJO) or the remnants of baroclinic activity in the mid-latitudes (Fig. 1b). Convective self-aggregation may be another potentially important mechanism[2,178].

Large-scale winds. Environmental winds advect the developing vortex, and thereby steer it, while interfering with its structure and energetics. Vertical wind variations, or wind shear, are intrinsic to all planetary atmospheres characterized by horizontal temperature gradients, and lead to time-mean atmospheric features, such as low-level subtropical anticyclonic flows (Fig. 2a) and upper-level zonal jets (Figs. 1b and 2b). Vertical shear is the major dynamical inhibitor of TC intensification as it acts against the formation of the coherent deep columns of high entropy air required for genesis. This shear dilutes entropy and thereby weakens convective updrafts and slows the surface winds required to extract heat from the ocean to fuel continued convection[179].

Planetary rotation. Two key scaling hypotheses exist for the dependence of TCs on the planet's rotation. Planetary rotation is manifest as the Coriolis parameter f ($=2\Omega\sin\phi$, where ϕ is the latitude and Ω the rotation rate of the planet), also called planetary vorticity. A first hypothesis predicts an f scaling, that is, all else ignored, TCs should become more frequent towards the poles[142]. The Coriolis parameter is zero at the equator and increases with latitude, which sets a meridional vorticity gradient (Fig. 1b). This gradient, the so-called the β effect, is also relevant:

$$\beta = \frac{\mathrm{d}f}{\mathrm{d}y} = \frac{2\Omega}{a}\cos\phi. \quad (1)$$

Here a is the planetary radius. Opposite to f, β is largest at the equator and zero at the poles. This gradient is what causes TC to move poleward and westward (the process known as beta drift) by establishing secondary 'beta gyre' circulations[180] on either side of the TC (Fig. 1b). Beta drift scales with the square root of β (ref. [181]). Consequently, westward TC tracks rapidly curve poleward in the tropics, but this effect diminishes at higher latitudes. β provides a non-climatological (that is, dependent on planetary size and rotation rate as opposed to mean climate) constraint on TC latitudes by limiting the size of cyclonic disturbances and hence reducing beta drift[144]. If TC radii are to increase with climate warming, as has been hypothesized[100], then we would expect stronger beta drifts.

Climatological convection. The majority of TCs (~70%) are spun out directly from climatological convection (Fig. 2a). The large-scale structure of this convection, which includes the ITCZ, can be deduced by combining two conceptual building blocks of tropical dynamics—convective quasi-equilibrium theory[182] and the weak temperature gradient approximation[183]—into a single framework[184]. This framework provides an explanation for the structure of large-scale convective circulations that result from time-mean spatial variations in MSE. Convective quasi-equilibrium theory abstracts that the upward flow of MSE into the subcloud boundary layer due to enthalpy fluxes (latent and sensible heat transfer from the ocean surface) is balanced by a downward transfer of low MSE air from the dry free troposphere through convective downdrafts and large-scale subsidence (Fig. 1b). Employing this balance, Emanuel[184] provides the following zeroth order diagnostic expression for controls on the strength of climatological convective updrafts in the ITCZ and Pacific Warm Pool:

$$M_\mathrm{u} \propto w + \frac{\mathrm{SEF}}{\Delta\mathrm{MSE}}, \quad (2)$$

where M_u is the average mass flux of the deep convective updrafts, w the tropical average vertical velocity at the top of the boundary layer, SEF the surface moist enthalpy fluxes, and ΔMSE the difference between the boundary layer MSE and free tropospheric MSE (per unit volume). The corresponding convective updrafts release local instabilities and transport MSE from the boundary layer into the free troposphere. Equation (2) implies that the horizonal distribution of updraft strength is constrained by horizonal variations in the surface fluxes, boundary layer MSE and free tropospheric MSE. As the atmospheric moisture content declines rapidly with altitude and the effect of latent heat flux dominates over that of sensible heat flux, the spatial distribution of climatological convection largely reflects surface evaporative fluxes and lower-level tropospheric moisture[185].

Behind GPIs is the assumption that climatological tropical cyclogenesis, approximated as genesis potential, is a localized process. This assumption therefore abstracts away the complex set of planetary, synoptic, and mesoscale processes that give rise to the observational distributions against which GPIs are calibrated. The problem is that processes resulting in cyclogenesis and intensification occur over a wide range of overlapping spatial and temporal scales and can be dislocated from one another[16,18–20] (see Extended Data Figs. 1 and 2 for examples). This issue probably gives rise to the aforementioned apparent limitations of GPIs. Thus, to generate a fundamental understanding of the physical controls over TC distribution with robust prognostic skill requires us to make explicit the links between the synoptic and mesoscale processes inherent to TCs and the large-scale dynamics within which they emerge, intensify and dissipate.

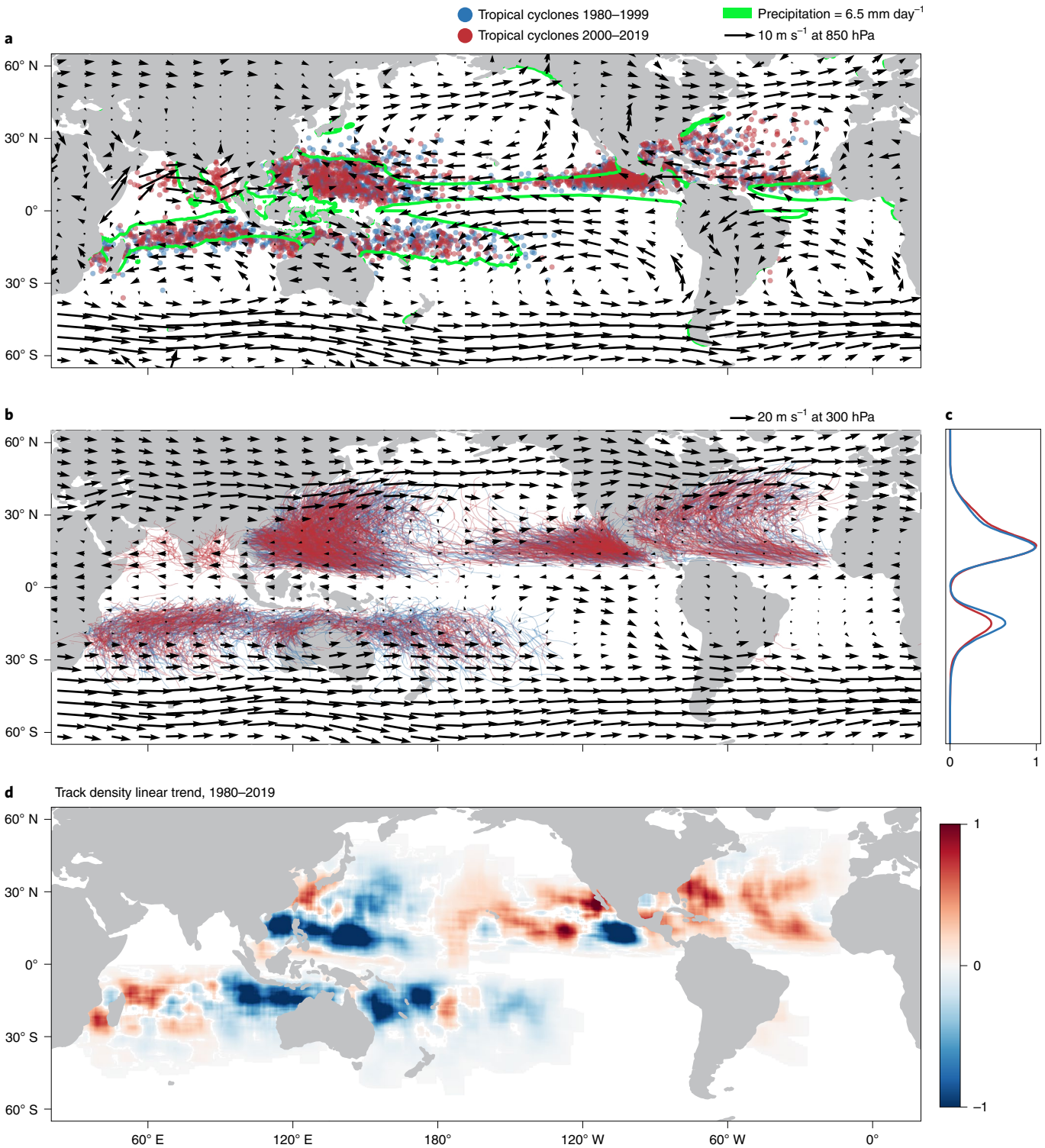

Fig. 2 | Planetary-scale atmospheric circulation, precipitation and TC activity. a, Seasonal mean precipitation (green contours), lower-tropospheric winds (arrows) and first recorded positions of disturbances that develop into TCs (blue/red dots). **b**, Upper tropospheric winds (arrows) and TC tracks (blue/red curves). **c**, Normalized zonal-mean TC track density (Methods) during 2000–2019 (red) and 1980–1999 (blue). **d**, TC track density linear trend (shading) over the period 1980–2019 (Methods), 1980–2019. The 6.5 mm day^{-1} contour in **a** corresponds to the 90th percentile seasonal mean precipitation and marks the region of tropical convection during the TC seasons. The underlying environmental fields from the Copernicus Climate Change Service[156] and TC data are from Knapp et al.[157]. Seasonal averages are computed for the months of peak TC activity: July, August, September and October in the Northern Hemisphere and January, February, and March in the Southern Hemisphere (Methods).

It is remarkable that the relationship between the convective mesoscale processes that underpin TCs and large-scale dynamical structures has been largely ignored[21,22] since the first GPI was published in 1979[7]. This is all the more striking because much observed TC genesis is embedded within belts of climatological convection that are very well studied: roughly 70% of the first recorded

TC positions occur within the ITCZ (inside the green contour in Fig. 2a). Idealized simulations, historical evidence, and palaeoclimatological reconstructions[23–25] have all found strong relationships between ITCZ characteristics and TC frequency.

Diversity in TC genesis mechanisms (Fig. 1) is part of this problem and presents a challenge to deriving a simple prognostic framework for TC genesis and intensification. Although TC genesis typically occurs in non-baroclinic large-scale environments, 30% of genesis events do involve baroclinic influence[26]. Globally, one in six TCs form via 'tropical transition', whereby transient upper tropospheric disturbances trigger deep convection and low-level moisture convergence on coinciding with lower tropospheric lows[27] (Fig. 1b and Extended Data Fig. 2). This process is possible over much lower sea surface temperatures (SSTs, <17 °C) and at higher latitudes (>40° N) than canonical TC genesis[28]. These upper tropospheric disturbances originate from anticyclonic wave breaking following planetary wave amplification and thus have a strong, established sensitivity to planetary warming[29]. GPIs computed at a higher frequency can capture some of these 'non-traditional' genesis pathways, including polar lows and Mediterranean warm-core cyclones[30] (Extended Data Fig. 3), but these routes are poorly captured by GPIs computed from monthly mean variables, as is done nearly universally. Critically, genesis pathways that are marginal in the present day may have been non-marginal in the past and may become non-marginal again as the planet warms[31–34].

Most non-canonical genesis pathways occur on the poleward edge of the modern TC distribution. On the equatorward side, convectively coupled equatorial waves (CCEWs), easterly waves and the Madden–Julian Oscillation (MJO) play a critical role in TC genesis and intensification[4]. This further complicates the analysis of climates' TC favourability. These synoptic and mesoscale convective atmospheric phenomena can all trigger convective aggregation, but also interact with each other in a number of ways[35]. CCEWs are estimated to be involved in ~85% of North Atlantic and western North Pacific TC genesis events[36,37], and enable the necessary convective organization for genesis[38]. However, this may simply determine the location and timing of genesis, not overall TC frequency[39]. Indirectly, CCEWs can condition the atmosphere to either encourage or suppress TC genesis locally as their convective anomalies modulate vorticity, temperature, moisture and wind shear at a range of scales. They also induce remote responses[40–42], such as far-field suppression of TC potential intensity (PI (Box 1)) via upper tropospheric temperature homogenization, which maintains weak horizontal temperature gradients in the tropics (the weak temperature gradient (Box 1)).

Past, present and potential latitudinal migrations

Palaeoclimate reconstructions and modelling. At geologic timescales, it is likely that the secular cooling throughout the Cenozoic (the past 66 Ma) resulted in the contraction of latitudes with both high genesis potential and PI towards the equator in both hemispheres (Fig. 3)[43]. This would have been coincident with a contraction of the Hadley circulation and equatorward shifts in the subtropical jet streams[43]. During the Early Eocene climate optimum (53–51 million years ago (Ma))—the warmest prolonged climate interval of the Cenozoic—palaeoproxies show atmospheric CO_2 concentrations of around 1,400 ppm (with a very large uncertainty range[44]). This may have resulted in the equator-to-pole temperature gradient being up to 10 °C flatter than it is in the modern era[45,46] and summertime surface continental temperatures in the Arctic reaching ~23 °C (ref. [47]). During the geologically brief Palaeocene–Eocene Thermal Maximum (PETM, ~55 Ma), these differences were likely even more exaggerated[48,49].

Although the circulation dynamics associated with the Eocene climate remain under debate[45,50], the available reconstructions and climate models forced by Eocene continental configuration and CO_2 concentrations suggest increased extratropical humidity, poleward jet stream shifts and Hadley circulation expansion relative to the present[43,47,51–53]. This implies a marked poleward expansion of areas favourable to TC formation and intensification (Fig. 3 and Extended Data Fig. 4). Eocene simulations show genesis potential centred on the subtropics (~25° latitude) in both hemispheres in contrast with that of the modern era, in which it dominates the deep tropics (~10° latitude)[34,43] (Fig. 3c). Moreover, a recent PETM simulation using a 25 km horizontal resolution atmospheric GCM shows a very strong suppression of low-latitude TCs, and both hemispheres' mid-latitudes (30–60° latitude) producing many TCs[34] (Fig. 3b). These results agree with cloud-system resolving simulations of an idealized Eocene-like climate[32] (Fig. 5, yellow line).

Contemporary TC distributions were probably established sometime towards the end of the warm Pliocene[43,54] (2.6–5.3 Ma). For most of this period, proxy-based reconstructions indicate atmospheric CO_2 concentrations of 350–450 ppm (ref. [55]), equator-to-pole SST gradients up to 5 °C flatter than the present one[56] and surface westerlies weaker and possibly more poleward[57]. In addition, Pliocene climate may have featured an expanded low-latitude warm pool, reduced equatorial and coastal upwelling, weakened Hadley circulation and TC activity enhanced and shifted poleward relative to that of the present[54,58–60]. During the late Pliocene, atmospheric CO_2 decline, among other factors, led to the establishment of colder climate patterns, which culminated with the onset of Northern Hemisphere glaciation[61]. This marked the start of a period, ending in the present century, when latitudinal variations in TC occurance became more muted and were primarily controlled by orbitally driven insolation changes and the resultant glacial cycles, shorter millennial climate variability and varying aerosol emissions.

GCMs forced with continental ice sheet reconstructions and low atmospheric CO_2 concentrations (185 ppm) indicate that the planet's TC distribution during the Last Glacial Maximum (21 thousand years ago (ka)) was not significantly different from that of the present day, albeit mean TC intensity was probably lower[62–64]. These models, however, disagree over the large-scale atmospheric circulation structure, specifically whether the Southern Hemisphere subtropical jet was poleward or equatorward relative to the modern day and whether atmospheric convection in the western Pacific was stronger or weaker[65,66]. Since the Last Glacial Maximum, multimillennial-scale TC variability was probably dominated by a slow increase in the boreal summer equator-to-pole insolation gradient until ~10 ka, and the subsequent decline associated with orbital precession[67]. The increased insolation gradient at the precession minima (~10 ka) may have caused amplified tropical convection and strengthened mid-latitude jets[68–71]. This seems to correspond with the suppressed genesis potential of the most equatorward TCs[67].

Orbitally driven variations were punctuated by millennial-scale abrupt climate changes, including the cold Heinrich and Younger Dryas events. The slowdown of the Atlantic meridional overturning

Fig. 3 | Changes in TC latitudinal distribution over geological timescales. a, Modern TC tracks, as in Fig. 2b—the blue curves correspond to the period 1980–1999 and red ones to 2000–2019. **b**, Simulated PETM TC tracks. **c**, Changes in simulated seasonal-mean genesis potential relative to pre-industrial throughout the Cenozoic. In **c**, the yellow strips indicate shifts in the hemispheres' maximum genesis potential latitudes and the green and blue columns mark their upper and lower bounds, respectively (defined as latitudes of 25% drop-offs on either side of the maxima). The data in **b** and **c** are based on GCM simulations[34,43,78] and hold large uncertainties. Red circles in **c** indicate the observed satellite era poleward TC migration of the modern era[94]. Pre-industrial TC LMI latitudes are 18° N and 16° S. Given the wide range in twenty-first century projections (see text), no future estimates are plotted.

circulation[72], typically associated with these events, cooled the North Atlantic, which suppressed PI[67]. The increased meridional temperature gradient in the Northern Hemisphere would have led to an intensification and equatorward shift of both the subtropical jet and Hadley cell[73,74], and presumably suppressed higher latitude TC genesis and intensification[67]. Changes in large-scale climate over

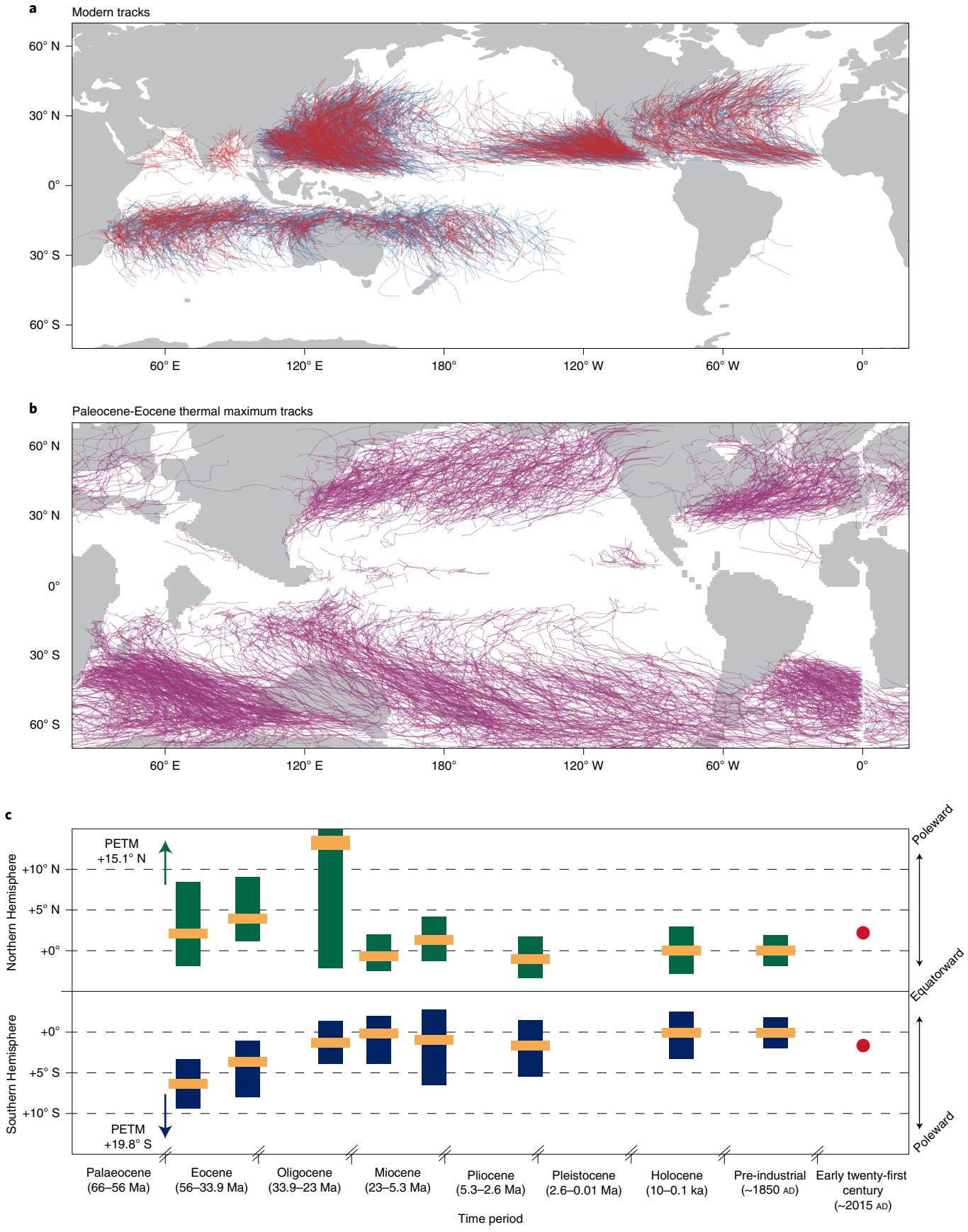

the past 21,000 years (CO_2 ~180–280 ppm) are probably small in comparison to changes driven by atmospheric CO_2 since the Eocene (CO_2 ~500–2000 ppm) and Pliocene (CO_2 ~300–500 ppm); in particular, mean ITCZ shifts since the Last Glacial Maximum were probably less than 1° latitude[75].

Atmospheric aerosols provide an additional control over TC occurrence on shorter timescales. They were suppressed during the 'green Sahara' period centred on the mid-Holocene[76,77] (6 ka), but sporadically increased after volcanic eruptions[25,78]. Mineral dust has hemispherically asymmetric impacts on temperature, and consequentially ITCZ location[79] and TC latitudes[25]. Further north, reductions in dust increases the SSTs, which results in PI increases and poleward jet shifts that expand regions of TC favourability[25,76,77]. Moreover, these North Atlantic TCs were probably shifted poleward relative to those at present, as the Sahara greening caused a poleward displacement of easterly waves[76,77].

Genesis potential and PI based on model simulations show no secular trends over the 2,000 years prior to the Industrial Revolution[78,80]. Integrated Atlantic palaeotempestological records (16–32° N), however, suggest a persistent poleward migration of eastern tropical Atlantic TCs over the last 450 years in concert with ITCZ poleward migration[81]. Other records show that TC activity shifted from the Caribbean and Gulf of Mexico towards the Bahamas and New England around AD 1400, correlated with warm central tropical Atlantic SSTs prior to this shift and a relatively warmer western North Atlantic afterwards[82]. This would have been coincident with high basin-integrated TC activity in the Medieval Warm Period (MWP, AD ~900–1450) followed by a lull during the Little Ice Age[83] (LIA, AD ~1450–1850). Palaeoreconstructions and historical evidence imply poleward western North Pacific TC and ITCZ shifts during the MWP and equatorward shifts during the LIA[24,84]. The North Atlantic poleward and western North Pacific equatorward TC shifts across the MWP–LIA transition occurred, presumably, with Pacific warm pool cooling, Pacific Walker circulation weakening, East Asian summer monsoon weakening and a narrowing and southward shift in the ITCZ[84,85]. Finally, tree rings suggest a secular twentieth century TC poleward migration in the western North Pacific (33–45° N)[86].

TC activity may also fluctuate with changes in the El Niño–Southern Oscillation (ENSO), Atlantic Multidecadal Variability (AMV) and Pacific Decadal Oscillation (PDO) over centennial and millennial timescales[83,87]. The MWP–LIA transition arguably marked an increase in ENSO amplitude, a change from a predominately negative to a predominately positive AMV and change from a persistent negative PDO state to a muted PDO signal (Hernandez et al.[88] review these modes throughout the Holocene). Most casual interpretations of TC latitudinal variability in the palaeorecords over centennial-to-millennial timescales are understood via connections to the ITCZ, often mediated by ENSO variability[24,81,89]. Further, TC coupling to large-scale stationary circulation features, such as the subtropical highs, is also recognized[25,81,90].

We stress that reconstructions of TCs throughout Earth's history suffer large uncertainties. Model biases and uncertainties in boundary conditions and radiative forcing diminish the utility of climate simulations and their genesis potential estimates—to which the aforementioned limitations in GPIs also apply. There is even a continued debate over how TCs are identified and tracked in these numerical simulations[13]. Conversely, proxy-based TC reconstructions only record local storm transits and are biased towards intense events near coastlines[91], whereas centennial variability in individual palaeorecords of intense TCs may be random and not reflective of large-scale climate dynamics[92]. Thus, synthesizing palaeohurricane records is important, yet complicated by very strong spatial undersampling[93].

Poleward TC migration in recent observations. Subtle but robust poleward trends of 53±43 and 62±48 km per decade[94] in TC seasonal-mean lifetime maximum intensity (LMI) latitudes are detectable in observations of the Northern and Southern hemispheres, respectively (1982 to 2012). Although these estimates are largely drawn from analyses of the International Best Track Archive for Climate Stewardship (IBTrACS) archive, which aggregates multiple records, such a poleward migration is found across different datasets and also for genesis latitudes[94–96]. The magnitudes of these trends depend on the period and TC intensity considered[94]. LMI is used as it does not rely on absolute intensity magnitudes, which are inconsistently recorded and poorly represented in reanalysis[94,97]. Dynamical reanalysis data reproduce TC LMI latitudes mostly within a few degrees of the observations[97]. However, simulated TCs tend to persist too long into high latitudes, where they expand radially and become better resolved, and thus achieve higher intensities there and distort higher latitude (>30°) LMI estimates[97]. Thus, satellite-based records provide the most reliable source for trends in TC latitudes.

Over half of the recently observed poleward migration trend is explained by interbasin frequency changes (Fig. 2d). This follows from the North Atlantic (average LMI 2,800 km from the equator versus hemispheric mean of 2,150 km) and South Pacific (1,990 km versus 1,900 km) increasingly producing more cyclones relative to other basins in their respective hemispheres[94,98]. Poleward migration is also not uniform over LMI latitude percentiles[96]—one of the most equatorward hurricanes on record occurred in 2016 (Hurricane Pali, ~2.3° N). These present-day trends appear to be associated with changes in both the ocean (SST patterns; Fig. 4a) and atmospheric thermodynamics (PI; Fig. 4b), and dynamics (vertical shear, large-scale tropospheric winds)[94,96,99]. Additionally, genesis potential has increased during this period (Fig. 4e). Twentieth-century global-mean SST increases may have forced increases in storm radii in the western North Pacific TCs[100]. These larger TCs tend to propagate further poleward following an increased beta drift (Box 1) and interaction with the subtropical highs and tropical upper tropospheric troughs[101]. The latitudinal displacement of western North Pacific TCs in particular has been associated with suppressed genesis during the late TC season linked to the Pacific Walker Circulation[102]. These poleward migration trends are coincident with the increased rates of observed extratropical transition[103].

In addition to the observed gradual poleward migration of the present day, pronounced transient zonal and meridional TC migrations occur in response to the ENSO, PDO and AMV cycles[104]. During negative PDO phases (warmer SSTs in the western and central subtropical Pacific), maximum PI latitudes extend poleward, which encourages higher latitude Pacific TC genesis[105]. The poleward migration of North Atlantic TCs associated with ENSO occurs after both dynamic and thermodynamic suppression of low-latitude TCs. During El Niño, Pacific Walker circulation weakening intensifies the upper-tropospheric westerlies over the North Atlantic, which amplifies the vertical wind shear over the Caribbean and eastern Northern Pacific[106,107]. Meanwhile CCEWs originating in the Pacific triggered by the anomalously warm temperatures there push the tropical North Atlantic atmosphere out of thermodynamic equilibrium with its underlying SSTs to suppress TC genesis[41].

Over the past three-to-four decades, the west–east equatorial SST gradient across the tropical Pacific has strengthened, with the eastern equatorial Pacific becoming colder and the western Pacific warmer, and correspondingly the Walker circulation has intensified[108–110]. This intensification may reflect a negative PDO phase with possible contributions from aerosol effects and a thermostat-like response to greenhouse gas forcing[110]. Transition to a positive AMV circa AD 2000[109,111] and greater interbasin temperature contrasts[108] have also been invoked to explain this strengthening of the Walker circulation. Regardless of the cause, the stronger Pacific Walker circulation has intensified vertical wind shear over the equatorial central Pacific and the deep tropical North Atlantic, and so has contributed to the observed recent TC poleward migration[98,111].

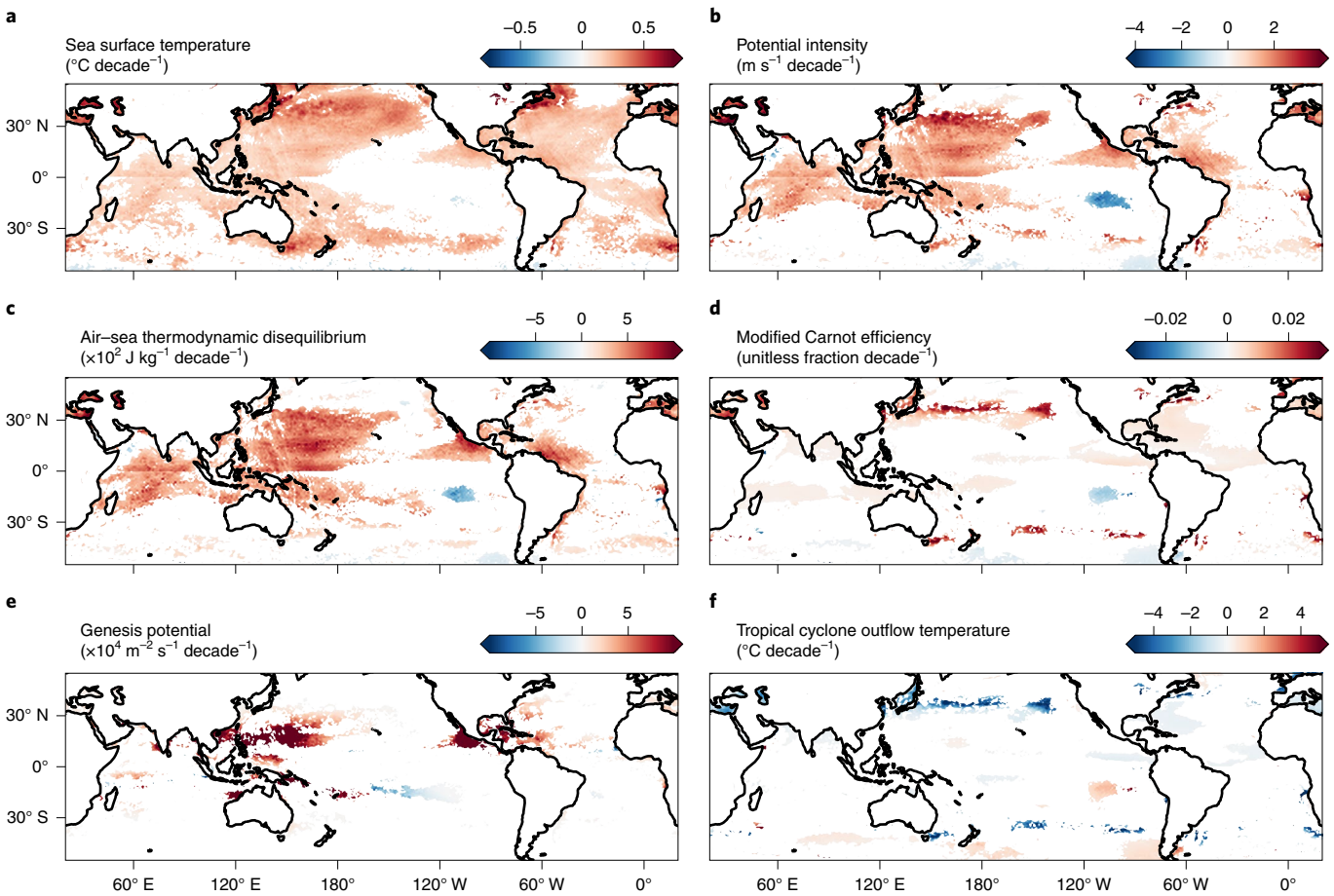

Fig. 4 | Recent linear trends in key thermodynamic variables that affect TCs and their genesis potential. a, SST trends. **b**–**d**, Trends in TC PI (Box 1) (**b**), in air–sea thermodynamic disequilibrium (**c**) and modified Carnot efficiency (**d**). The latter two variables regulate trends in PI (Box 1 and Methods). Thermodynamic disequilibrium represents the main heat source for TCs. Carnot efficiency represents the maximum efficiency at which the atmosphere can use the available heat to maintain TC winds. **e**, Trends in genesis potential. **f**, Trends in TC outflow temperature, which controls trends in Carnot efficiency. See Methods for the calculation of these variables. As for Fig. 2, seasonal averages are computed for the months of peak TC activity. The underlying environmental fields are from ERA5 data[156], and trends are computed for 1980–2019. Only values with $P < 0.05$ are plotted.

In contrast, by the century's end, a relaxation of the SST gradient across the Pacific, with a pronounced eastern equatorial Pacific warming and corresponding weakening of the Walker circulation, is projected in nearly all Climate Model Intercomparison Project Phase 6 (CMIP6) models[110]. All else being equal, this would correspond to lower vertical wind shear over the equatorial central Pacific and equatorial North Atlantic, and an equatorward ITCZ shift that would encourage low-latitude TC formation and intensification.

Simulated climate change. Idealized aquaplanet TC simulations (no continents (reviewed by Merlis and Held[23])) have been conducted with atmospheric models and fixed SSTs or with a simplified 'slab–ocean' representation of fixed oceanic heat transport (via the 'q flux' abstraction). These simulations generally neglect zonal climate asymmetries and the seasonal cycle, and have other limitations. For example, only models with a dynamic oceanic heat transport can provide a strong negative feedback on ITCZ displacements. Consequentially, changes in the ITCZ position and strength under variable climatic forcing differ dramatically between aquaplanet and fully coupled simulations—in the former, the ITCZ can move poleward by 10–20° latitude, whereas in the latter the ITCZ intensity changes, but its shifts do not exceed ~1° (ref. [112]). In addition, aquaplanet ITCZs are sensitive to model resolution and convective parameterization[113].

Nevertheless, aquaplanet simulations with imposed atmospheric cross-equatorial heat transport variations suggest a TC genesis scaling of a 40% increase in global TC frequency per degree of latitude of poleward ITCZ shift[114]. However, increases in TC genesis can occur on warming aquaplanets even with an equatorward ITCZ shift as changes in the subtropical jet and reductions in mid-latitude baroclinicity increase the likelihood of TC genesis (Fig. 5). Aquaplanet TC activity appears to be correlated with atmospheric static stability, but it is only sensitive to vertical shear above a certain threshold value (~5 m s^{-1} (ref. [115])). The climatological relationship of TC latitudes with PI seems to be weak and non-monotonic[31,32,115]. Rather, poleward migrations reflect the aerial expansion of high (>70 m s^{-1}) PI values. These poleward migrations follow tropical expansion, but not simply the concurrent dilation of the Hadley circulation[33].

Full continent slab–ocean statistical downscaling experiments with large CO_2 increases (×8 and ×32 pre-industrial concentrations) show LMI poleward migration (1.6 and 7.4°, respectively) and prolonged TC lifecycles[31]. The overall maximum PI does not increase with these hyperexaggerated warmings (consistent with Walsh et al.[115]). This statistical downscaling method involves inserting $O(10^6)$ artificial random weak vorticity anomalies (referred to as TC 'seeds') over the global ocean in an effort to simulate realistic pre-TC disturbances, which—as we stress above—may come

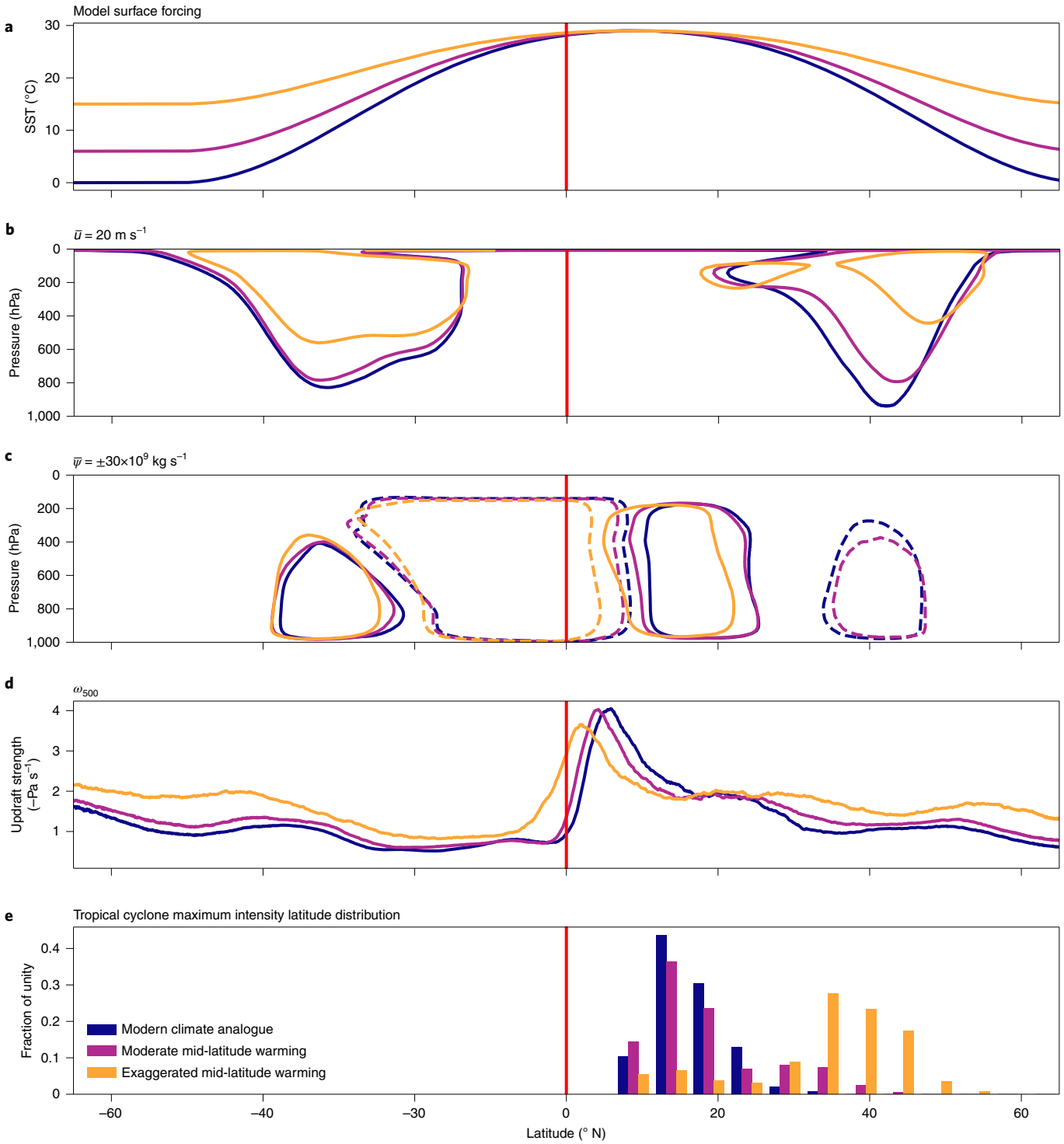

Fig. 5 | Large-scale circulations and TC latitudinal distributions under idealized climate warming scenarios in cloud-system-resolved aquaplanet simulations. a, The model is forced by three fixed SST meridional profiles that range from contemporary climate (blue) to moderate mid-latitude warming (purple) to exaggerated Eocene-like warming (orange). **b**, $\bar{u} = 20\,\mathrm{m\,s^{-1}}$ zonal velocity contours that mark the jet streams. **c**, $\bar{\Psi} = \pm 30 \times 10^9\,\mathrm{kg\,s^{-1}}$ streamlines of the Hadley and Ferrel cells. **d**, Mean updraft strength measured as the time mean of the zonal maximum pressure velocity at 500 hPa multiplied by −1. **e**, Divergent influences lead to the northward shift of TC LMI distribution (despite non-monotopic changes at low latitudes). Data from Fedorov et al.[32], who also found that GPI calculations underestimate the magnitude of the mid-latitude genesis response to warming.

from a number of spatially and temporally variable processes, potentially poorly resolved in GCMs (Fig. 1 and Box 1). Most of these artificial vorticity anomalies decay rapidly, but a few survive and are then passively advected by the large-scale winds and beta drift. Computing the thermodynamics of these vortices yields the corresponding TC lifecycle (that is, the progression through genesis, intensification and cyclolysis; this methodology does not represent extratropical transition). The results from this approach depend on the number of seeds used and thus this method requires calibration to reproduce a realistic TC frequency[116].

Some coupled ×2 and ×4 CO_2 experiments with dynamically simulated TCs exhibit small poleward shifts of several degrees latitude in the Northern Hemisphere[117], but other coupled ×2 CO_2 experiments found zonal, but not poleward, TC migration[16]. Vecchi et al.[16] found that in these experiments the pre-TC synoptic and convective mesoscale disturbances, defined as the seasonal variance in 3–10 day bandpassed 850 hPa vorticity, are the principle atmospheric drivers of TC frequency responses in increasing atmospheric CO_2 simulations. Such TC source disturbances are found to be highly concentrated within climatological convection (the ITCZ and Pacific Warm Pool) with potential links between their frequency and time-mean local tropospheric pressure velocity, $\bar{\omega}$ (ref. [1]). This approach contrasts with that of statistical downscaling methods, which assume a constant number of TC seeds (the artificially inserted pre-TC source disturbances), but does not invalidate the random seeding approach as long as the seeds are sufficiently weak and numerous.

Attribution work using coupled models found that recent TC distribution changes are very probably anthropogenically forced[118]. However, CMIP5 models and various regional downscaling experiments project a range of twenty-first century TC migration scenarios from no further migration to poleward LMI migration of a few degrees (but less than the 5° latitude implied by a continuation of the 0.5° per decade trend[94]) and zonal migration of Pacific TCs[119,120]. Early analysis of CMIP6 has found no consensus on twenty-first century distribution changes in explicitly resolved TCs[13], but statistical downscaling shows a poleward migration in the Northern Hemisphere, particularly in the North Atlantic[11]. Climate models' dynamically resolved TC activity is projected to be globally suppressed by greenhouse gases; however, statistical downscaling predicts increases in line with monthly-mean GPI values that reflect increasing PI and decreasing wind shear tempered against increasing mid-tropospheric relative dryness[11,12,121].

Some broad patterns in end-of-century TC predictions are established, although the statistical reliability of these findings depends on the selection of climate models studied. In the Northern Hemisphere, TC poleward shifts of a few degrees in the North Atlantic and both sides of the North Pacific alongside the suppression of the most western of the Pacific TCs are found in some but not all studies[103,122,123]. This is accompanied by a shift in Pacific TC activity towards the central Pacific[124] and increasing recurvature of the western North Pacific TC tracks[119,125]. Southern Hemisphere projections show no clear deviation in TC genesis latitudes between the current and future climate[11,120]. However, statistical downscaling of CMIP6 models shows a significant poleward expansion of TC activity both in the North Atlantic and the South Indian oceans[11]. All these projections of increased high-latitude TC activity under greenhouse warming are consistent with other projections of increased rates and intensity of extratropical transition in the western North Pacific and North Atlantic[126–128]. Additionally, TC translation speed is projected to decrease over the twenty-first century, following poleward shifts in the mid-latitude westerlies, which would increase the mid-latitude TC track density[129].

Although GCMs do reproduce modern TC climatologies reasonably well, strong errors persist, particularly at the distribution edges[118–120]. Models overestimate the historical genesis rates in the central North Pacific and the Southern Hemisphere, but underestimate eastern North Pacific and North Atlantic TCs[11,13,130]. Although SST patterns are considered the principal cause behind spreads in projected TC climatologies[12,16], this implicates a complex set of processes, such as the slowdown of the Atlantic meridional overturning circulation and radiative feedbacks. Moreover, intermodel spread in projected SSTs cannot account entirely for the lack of inter-model consensus and another likely factor is differences in models' representations of atmospheric deep convection[130,131].

Linking mesoscale physics to large-scale climate dynamics

An emergent hypothesis for explaining recent TC poleward migration relates it to the observed tropical expansion through the areal expansion of low vertical wind shear and high PI regions of the subtropics[94]. This invokes changes in the latitudes of the descending branches of the Hadley circulation and mid-latitude jet streams. PI has increased in recent decades (Fig. 4b) and model simulations indicate that changes in TC distribution track the aerial expansion of high PI values[78,115]. Such an expansion, which follows from local increases in modified Carnot efficiency and lower TC outflow temperatures (Box 1), is present in the recent record (Fig. 4d,f). These results broadly agree with the Eocene and Pliocene model reconstructions, which show wider tropics during those epochs coincident with a higher latitude TC activity. However, assumptions of tropical expansion causally driving TC poleward migration require careful examination[33]. As the limitations of GPIs and existing frameworks have shown, the challenge lies in integrating the sensitivity of convective mesoscale processes to planetary temperature with the summertime mean circulation's broader sensitivities, which include jet stream shifts, Hadley cell expansion and ITCZ changes[132–134], each driven by their own distinct set of dynamics.

One major confounding aspect of process-based understanding of the recent subtropical decrease in vertical wind shear and increase in PI[94] is the link—or lack thereof—between changes in the Hadley cells and the subtropical jet. A ~0.5° per decade poleward expansion of the Hadley cells, normally shorthand for 'the tropics', can be identified in several metrics and datasets[133]. However, no robust trend has been found for the subtropical jet[135], despite the expectation that they would covary because the subtropical jet enables strong vertical wind shear and the Hadley cell terminates where the shear is maximal[136]. The much weaker poleward trend, if any, in the subtropical jet implies that different aspects of tropical expansion are only partially coupled[137].

The latitude of the Hadley cell edge is, however, negatively correlated on interannual timescales, at least in CMIP5 models, with the strength (not latitude) of the subtropical jet[138]. Furthermore, the coherent mid-latitude jet stream in the time-mean zonal-mean circulation represents the superposition of two distinct, yet dynamically connected, features: the subtropical jet and the eddy-driven jet at higher latitudes. The Hadley cell edge was shown to be positively correlated with the latitude of the eddy-driven jet[139], but not of the subtropical jet. Although mid-latitude baroclinicity associated with the eddy-driven jet is relatively weak during TC seasons, it still produces consequential wind shear[140]. How this relationship between the Hadley cell edge, eddy-driven jet latitude and subtropical jet strength affects the synoptic and mesoscale processes of baroclinically enabled TC genesis[26], intensification, and extratropical transition (Fig. 1b) remains a pressing open research question. Indeed, this type of TC genesis becomes common in the mid-latitudes of idealized models simulating warm climates[31–34], in particular when the two jets split (Fig. 5 and Extended Data Fig. 5). In these simulations, the summertime subtropical jet shifts equatorward, whereas the eddy-driven jet shifts poleward.

A separate explanation for recent TC poleward migration invokes suppressed genesis in the deep tropics caused by increased dry static stability in the warming tropical atmosphere[99] (Fig. 4a). However, the extent to which changes in the time-mean static stability effect actual TC processes is unclear. We suggest that static stability is best viewed as a co-factor with PI because both are related to atmospheric lapse rates. In fact, concurrent observations exhibit long-term increases in higher-frequency CCEWs[141] and increases in ITCZ precipitation (Extended Data Fig. 6), which contradicts the assertion that increased time-mean static stability implies less convective activity. Besides, SST increases in the deep tropics also lead to both a greater mid-tropospheric 'saturation deficit'

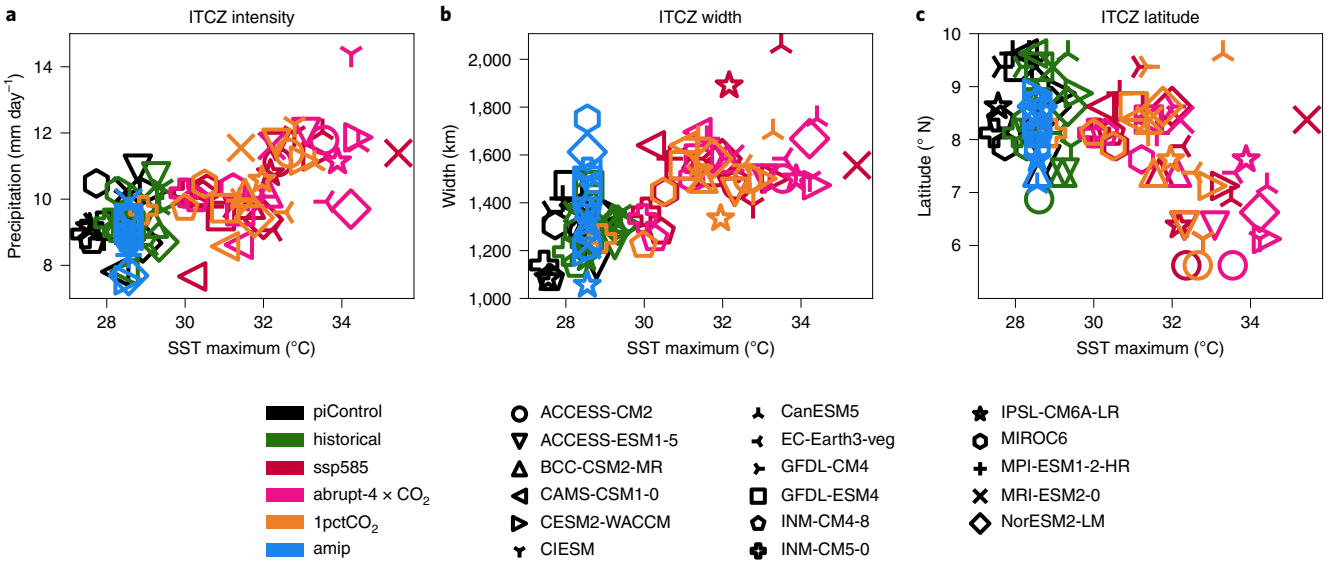

Fig. 6 | Changes in the Northern Hemisphere ITCZ under different warming scenarios in CMIP6. a–c, ITCZ intensity (**a**), width (**b**), and latitudinal position (**c**). For higher tropical SSTs, as predicted for the twenty-first century, climate models predict a stronger and broader ITCZ that is shifted towards the equator (Methods and see Extended Data Fig. 7 for changes in the Southern Hemisphere). Data from refs. [158–174].

(or tropospheric dryness relative to the boundary layer), a well-established thermodynamic TC inhibitor[116,142], and potentially to poleward shifts in the mid-latitude westerlies[134], which would most probably correspond to an aerial expansion of favourable TC latitudes with a high PI and lower vertical shear.

Another core aspect in discussions of TCs and climate change is ITCZ migration and dynamics, even though ITCZ responses to warming may depend on the metric considered and have been muted during recent climate change[132]. Despite large intermodel differences, overall precipitation responses in CMIP6 models show a stronger, wider, and equatorward ITCZ by the end of the twenty-first century (Fig. 6 and Extended Data Fig. 7), which follows changes in SST patterns and constraints from the Clausius–Clapeyron relation (the 'wet gets wetter' paradigm[143]). However, unlike the precipitation-based metrics used here, circulation measures computed in the previous CMIP5 models showed only small ITCZ latitudinal changes, with a muted narrowing and weakening[132]. Reconciling these differences is critical to understanding changes in low-latitude TCs in the twenty-first century.

Idealized simulations have confirmed that the further off-equator the ITCZ is, more ambient vorticity is available for TC genesis[1,144]. The wider and stronger it is by precipitation measures, the higher the free tropospheric specific humidity is likely to be[23]. Lastly, experiments with the moist shallow water equations indicate that a more poleward ITCZ is more susceptible to barotropic instability[145]. All these factors would enhance TC genesis, but how these idealized inferences of TC dynamics relate to more realistic ITCZs, and GCM biases, is not yet fully examined.

Changes at both the tropical–extratropical margin and within the ITCZ also raise questions about the degree of independence between source disturbances for TCs and the mature vortices themselves. For example, suppressing easterly waves in the North Atlantic, the primary source of pre-TC disturbances there, may alter the location and timing of genesis, but not overall TC frequency[39]. Moreover, the stronger the ITCZ is by circulation measures, the more initial disturbances may be available for TC genesis[117]. However, the ITCZ is strong and well defined in the central North Pacific where TC genesis is sparse (Fig. 2a), which confirms that the climatologies of source disturbances and TC development can be dislocated since this region can be a source of TC precursors.

Indeed, convective organization is possible through multiple pathways, such as CCEWs, the MJO, easterly waves, barotropic ITCZ breakdown, convective self-aggregation and, in the Indian Ocean, orographically induced vortices[2,32,146–148] (Fig. 1b). Yet, investigating the resultant pre-TC disturbances with contemporary climate GCMs is problematic because these models struggle to propagate convective disturbances realistically due to their time-space mismatch between the surface wind convergence and precipitation patterns caused by convective parameterizations[149]. As the realism of model simulations improves, it will become possible to ask: What is the best way to identify these pre-TC convective disturbances? How strongly are these disturbances linked to CCEWs? What are the climate sensitivities of these waves and disturbances? How are they affected by changes in ITCZ latitude, width, and strength?

Although the previous paragraphs discuss the potential links between convective mesoscale processes and large-scale atmospheric circulation, changes in the thermodynamic contribution to TC genesis and intensification favourability are also critical. These are probably most strongly tied to SST changes with greenhouse warming as PI increases in a pattern not dissimilar to that of tropical SST changes (compare Fig. 4a,b), which may be related to the recent time-mean enthalpy flux increase (Extended Data Fig. 8)[111]. At the same time, as most atmospheric moisture is contained within the lower troposphere and this content grows exponentially following the Clausius–Clapeyron scaling, the lower levels gain more water vapour with warming than the free troposphere does. The resultant increase in the relative dryness of the free troposphere (with respect to the boundary layer) discourages genesis[116]. This effect could be the strongest thermodynamic control over TC formation in a warming climate[11], but as moisture in the free troposphere is not controlled by the weak temperature gradient, it can vary across longitudes and depends on the large-scale tropical circulation (Box 1).

This entire discussion is focused on how the synoptic and mesoscale processes critical to the TC lifecycle respond to climate change as manifested in the time-averaged planetary-scale fields. We have neglected consideration of the feedbacks of TCs on the climate itself. Three particular effects are noteworthy: the effect of TCs in drying the free troposphere[3], the role of TCs in upper ocean mixing and oceanic heat transport[3,54,150,151], and low-cloud suppression by TCs[152]. These effects are not well handled by GCMs and may

appreciably affect their responses to radiative forcing, especially in the palaeocontext[54,151].

Implications for twenty-first century warming

The contemporary distribution of TCs was probably established during the late Pliocene around 3 Ma and has been slightly modulated since then by glacial cycles on orbital timescales, abrupt climate changes on millennial timescales, gradual aerosol variations, and volcanism on subdecadal timescales. The warm Pliocene (atmospheric CO_2 ~400 ppm) and warmer Eocene (~1,000 ppm) epochs probably produced TCs at substantially higher latitudes than those of the pre-industrial climate (~280 ppm). However, recent studies are divided as to whether twenty-first century levels of atmospheric CO_2 (400–1,000 ppm) (ref. [153]) will, indeed, result in a continuation of the present poleward trend in TC activity, as implied by those past warm climates.

Since at least the 1970s, the planet's TC distribution has unambiguously altered, evidenced in a poleward migration in latitudes of peak TC intensity at a rate of ~0.5° latitude per decade. This subtle but robust poleward shift has occurred during an expansion of the tropics at approximately the same rate, but during a period of stable latitudes of the ITCZ and subtropical jet. During the twenty-first century, in response to increasing atmospheric CO_2, the global ITCZ may become stronger but move closer to the equator (Fig. 6). The effects of this change on low-latitude TCs are ambiguous because a stronger ITCZ implies more convective mesoscale disturbances that could form into TCs, as well as higher free tropospheric humidity to fuel their intensification, but also implies less planetary vorticity available for them to acquire rotation and axisymmetric structure. Furthermore, these longitudinally averaged changes are dominated by the Pacific, where the eastern equatorial Pacific warming pattern is expected to emerge during the twenty-first century. This will have the effect of drawing some of the TC genesis away from the western and eastern Pacific towards the central Pacific. In the North Atlantic, changes in the favourability of baroclinic non-traditional TC genesis, vertical wind shear and ITCZ will be controlled by polar-amplified ocean warming (favourable to a TC poleward shift), possibly moderated by a weakening of the Atlantic meridional overturning circulation (generally favourable to a TC equatorward shift).

Further tropical expansion is likely, primarily driven by amplified warming in the tropical troposphere's upper levels, but will be constrained by the patterns of surface warming. Crucially, new modelling of TCs at the changing tropical–extratropical margin suggests that genesis and intensification between 30 and 40° latitudes could contribute materially to the TC climatology of the twenty-first century. Meanwhile, deep-tropical TCs will remain a critical feature of Earth's climate, most clearly following the anticipated equatorward ITCZ shift. Thus, we conclude that TCs will most probably occupy a broader range of latitudes by the end of the twenty-first century than during the pre-industrial period and the last three million years following equatorward ITCZ shifts and continued increasing mid-latitude favourability. We propose that the bleeding-edge research questions critical to address uncertainties in twenty-first century TCs are all centred around evaluating the dynamical links between the convective mesoscale processes of TCs and the better-understood large-scale warming sensitivities of the atmosphere and ocean. Potential feedbacks from TCs to the climate is another broad avenue for research.

Online content

Any methods, additional references, Nature Research reporting summaries, source data, extended data, supplementary information, acknowledgements, peer review information; details of author contributions and competing interests; and statements of data and code availability are available at https://doi.org/10.1038/s41561-021-00859-1.

Received: 15 April 2020; Accepted: 28 October 2021;
Published online: 29 December 2021

References

1. Hsieh, T., Vecchi, G. A., Yang, W., Held, I. M. & Garner, S. T. Large-scale control on the frequency of tropical cyclones and seeds: a consistent relationship across a hierarchy of global atmospheric models. *Clim. Dyn.* **55**, 3177–3196 (2020).
2. Boos, W. R., Fedorov, A. & Muir, L. Convective self-aggregation and tropical cyclogenesis under the hypohydrostatic rescaling. *J. Atmos. Sci.* **73**, 525–544 (2016).
3. Emanuel, K. 100 years of progress in tropical cyclone research. *Meteorol. Monogr.* **59**, 15.1–15.68 (2018).
4. Tang, B. H. et al. Recent advances in research on tropical cyclogenesis. *Trop. Cyclone Res. Rev.* **9**, 87–105 (2020).
5. Shaw, N. in *Hurricanes and Tropical Revolving Storms* Geophysical Memoirs No. 19 (ed. Newnham E. V.) 218 (Met Office, 1922); https://digital.nmla.metoffice.gov.uk/IO_8b3319c1-b2f3-47ce-a9c0-f77c445dad6f/
6. Knutson, T. et al. Tropical cyclones and climate assessment: part II: projected response to anthropogenic warming. *Bull. Amer. Meteorol. Soc.* **101**, E303–E322 (2020).
7. Gray, W. M. in *Meteorology over the Tropical Oceans* (ed. Shaw, D. B.) 155–218 (Royal Meteorological Society, 1979).
8. Emanuel, K., Ravela, S., Vivant, E. & Risi, C. A statistical deterministic approach to hurricane risk assessment. *Bull. Am. Meteor. Soc.* **87**, 299–314 (2006).
9. Camargo, S. J. & Wing, A. A. Tropical cyclones in climate models. *WIREs Clim. Change* **7**, 211–237 (2016).
10. Emanuel, K. Downscaling CMIP5 climate models shows increased tropical cyclone activity over the 21st century. *Proc. Natl Acad. Sci. USA* **110**, 12219–12224 (2013).
11. Emanuel, K. Response of global tropical cyclone activity to increasing CO_2: results from downscaling CMIP6 models. *J. Climate* **34**, 57–70 (2021).
12. Knutson, T. R. et al. Global projections of intense tropical cyclone activity for the late twenty-first century from dynamical downscaling of CMIP5/RCP4.5 scenarios. *J. Climate* **28**, 7203–7224 (2015).
13. Roberts, M. J. et al. Projected future changes in tropical cyclones using the CMIP6 HighResMIP multimodel ensemble. *Geophys. Res. Lett.* **47**, e2020GL088662 (2020).
14. Vidale, P. L. et al. Impact of stochastic physics and model resolution on the simulation of tropical cyclones in climate GCMs. *J. Climate* **34**, 4315–4341 (2021).
15. Lee, C.-Y., Camargo, S. J., Sobel, A. H. & Tippett, M. K. Statistical–dynamical downscaling projections of tropical cyclone activity in a warming climate: two diverging genesis scenarios. *J. Climate* **33**, 4815–4834 (2020).
16. Vecchi, G. A. et al. Tropical cyclone sensitivities to CO_2 doubling: roles of atmospheric resolution, synoptic variability and background climate changes. *Clim. Dyn.* **53**, 5999–6033 (2019).
17. Camargo, S. J. et al. Characteristics of model tropical cyclone climatology and the large-scale environment. *J. Climate* **33**, 4463–4487 (2020).
18. Sugi, M. et al. Future changes in the global frequency of tropical cyclone seeds. *SOLA* **16**, 70–74 (2020).
19. Ramsay, H. A., Singh, M. S. & Chavas, D. R. Response of tropical cyclone formation and intensification rates to climate warming in idealised simulations. *JAMES* **12**, e2020MS002086 (2020).
20. Yamada, Y. et al. Evaluation of the contribution of tropical cyclone seeds to changes in tropical cyclone frequency due to global warming in high-resolution multi-model ensemble simulations. *Prog. Earth Planet. Sci.* **8**, 11 (2021).
21. Knutson, T. R. et al. Tropical cyclones and climate change. *Nat. Geosci.* **3**, 157–163 (2010).
22. Walsh, K. J. E. et al. Tropical cyclones and climate change. *WIREs Clim. Change* **7**, 65–89 (2016).
23. Merlis, T. M. & Held, I. M. Aquaplanet simulations of tropical cyclones. *Curr. Clim. Change Rep.* **5**, 185–195 (2019).
24. Chen, H.-F. et al. China's historical record when searching for tropical cyclones corresponding to Intertropical Convergence Zone (ITCZ) shifts over the past 2 kyr. *Clim. Past* **15**, 279–289 (2019).
25. Pausata, F. S. R. & Camargo, S. J. Tropical cyclone activity affected by volcanically induced ITCZ shifts. *Proc. Natl Acad. Sci. USA* **116**, 7732–7737 (2019).
26. McTaggart-Cowan, R., Galarneau, T. J. Jr., Bosart, L. F., Moore, R. W. & Martius, O. A global climatology of baroclinically influenced tropical cyclogenesis. *Mon. Weather Rev.* **141**, 1963–1989 (2013).
27. Davis, C. A. & Bosart, L. F. Baroclinically induced tropical cyclogenesis. *Mon. Weather Rev.* **131**, 2730–2747 (2003).
28. Bentley, A. M. & Metz, N. D. Tropical transition of an unnamed, high-latitude, tropical cyclone over the eastern North Pacific. *Mon. Weather Rev.* **144**, 713–736 (2016).

29. Thorncroft, C. D., Hoskins, B. J. & McIntyre, M. E. Two paradigms of baroclinic-wave life-cycle behaviour. *Q. J. Meteorol. Roy. Soc.* **119**, 17–55 (1993).
30. Romero, R. & Emanuel, K. Climate change and hurricane-like extratropical cyclones: projections for North Atlantic polar lows and medicanes based on CMIP5 models. *J. Climate* **30**, 279–299 (2017).
31. Korty, R. L., Emanuel, K. E., Huber, M. & Zamora, R. A. Tropical cyclones downscaled from simulations with very high carbon dioxide levels. *J. Climate* **30**, 649–667 (2017).
32. Fedorov, A., Muir, L., Boos, W. R. & Studholme, J. Tropical cyclogenesis in warm climates simulated by a cloud-system resolving model. *Clim. Dyn.* **52**, 107–127 (2019).
33. Zhang, G., Silvers, L. G., Zhao, M. & Knutson, T. R. Idealized aquaplanet simulations of tropical cyclone activity: significance of temperature gradients, Hadley circulation, and zonal asymmetry. *J. Atmos. Sci.* **78**, 877–902 (2021).
34. Kiehl, J. T., Zarzycki, C. M., Shields, C. A. & Rothstein, M. V. Simulated changes to tropical cyclones across the Paleocene–Eocene Thermal Maximum (PETM) boundary. *Paleogeogr. Paleoclimatol. Palaeoecol.* **572**, 110421 (2021).
35. Yang, G.-Y., Methven, J., Woolnough, S., Hodges, K. & Hoskins, B. Linking African easterly wave activity with equatorial waves and the influence of Rossby waves from the Southern Hemisphere. *J. Atmos. Sci.* **75**, 1783–1809 (2018).
36. Russell, J. O., Aiyyer, A., White, J. D. & Hannah, W. Revisiting the connection between African easterly waves and Atlantic tropical cyclogenesis. *Geophys. Res. Lett.* **44**, 587–595 (2017).
37. Wu, L. & Takahashi, M. Contributions of tropical waves to tropical cyclone genesis over the western North Pacific. *Clim. Dyn.* **50**, 4635–4649 (2018).
38. Thorncroft, C. D. & Hodges, K. I. 2001: African easterly wave variability and its relationship to Atlantic tropical cyclone activity. *J. Climate* **14**, 1166–1179 (2001).
39. Patricola, C. M., Saravanan, R. & Chang, P. The response of Atlantic tropical cyclones to suppression of African easterly waves. *Geophys. Res. Lett.* **45**, 471–479 (2018).
40. Sardeshmukh, P. D. & Hoskins, B. J. The generation of global rotational flow by steady idealised tropical divergence. *J. Atmos. Sci.* **45**, 1228–1251 (1988).
41. Tang, B. H. & Neelin, D. J. ENSO influence on Atlantic hurricanes via tropospheric warming. *Geophys. Res. Lett.* **31**, L24204 (2004).
42. Vecchi, G. A. & Soden, B. J. Effect of remote sea surface temperature change on tropical cyclone potential intensity. *Nature* **450**, 1066–1070 (2007).
43. Yan, Q., Korty, R., Zhang, Z. & Wang, H. Evolution of tropical cyclone genesis regions during the Cenozoic era. *Nat. Commun.* **10**, 3076 (2019).
44. Anagnostou, E. et al. Changing atmospheric CO_2 concentration was the primary driver of early Cenozoic climate. *Nature* **533**, 380–384 (2016).
45. Evans, D. et al. Eocene greenhouse climate revealed by coupled clumped isotope-Mg/Ca thermometry. *Proc. Natl Acad. Sci. USA* **115**, 1174–1179 (2018).
46. Cramwinckel, M. J. et al. Synchronous tropical and polar temperature evolution in the Eocene. *Nature* **559**, 382–386 (2018).
47. Van Dijk, J. et al. Spatial pattern of super-greenhouse warmth controlled by elevated specific humidity. *Nat. Geosci.* **13**, 739–744 (2020).
48. Evans, D., Wade, B. S., Henehan, M., Erez, J. & Muller, W. Revisiting carbonate chemistry controls on planktic foraminifera Mg/Ca: implications for sea surface temperature and hydrology shifts over the Paleocene–Eocene Thermal Maximum and Eocene–Oligocene transition. *Clim. Past* **12**, 819–835 (2016).
49. Frieling, J. et al. Extreme warmth and heat-stressed plankton in the tropics during the Paleocene–Eocene Thermal Maximum. *Sci. Adv.* **3**, e1600891 (2017).
50. Huber, M. & Caballero, R. The early Eocene equable climate problem. *Clim. Past* **7**, 603–633 (2011).
51. Carmichael, M. J. et al. A model–model and data–model comparison for the early Eocene hydrological. *Clim. Past* **12**, 455–481 (2016).
52. Baatsen, M. et al. The middle to late Eocene greenhouse climate modelled using the CESM 1.0.5. *Clim. Past* **16**, 2573–2597 (2020).
53. Lunt, D. J. et al. DeepMIP: model intercomparison of early Eocene climate optimum (EECO) large-scale climate features and comparison with proxy data. *Clim. Past* **17**, 203–227 (2021).
54. Fedorov, A. V., Brierley, C. M. & Emanuel, K. E. Tropical cyclones and permanent El Niño in the early Pliocene epoch. *Nature* **463**, 1066–1070 (2010).
55. Martínez-Botí, M. A. et al. Plio-Pleistocene climate sensitivity evaluated using high-resolution CO_2 records. *Nature* **518**, 49–54 (2015).
56. Fedorov, A. V. et al. Patterns and mechanisms of early Pliocene warmth. *Nature* **496**, 43–49 (2013).
57. Abell, J. T., Winckler, G., Anderson, R. F. & Herbert, T. D. Poleward and weakened westerlies during Pliocene warmth. *Nature* **589**, 70–74 (2021).
58. Brierley, C. M. et al. Greatly expanded tropical warm pool and weakened Hadley circulation in the early Pliocene. *Science* **323**, 1714–1718 (2009).
59. Yan, Q. et al. Enhanced intensity of global tropical cyclones during the mid-Pliocene warm period. *Proc. Natl Acad. Sci. USA* **113**, 12963–12967 (2016).
60. Haywood, A. M. et al. The Pliocene Model Intercomparison Project Phase 2: large-scale climate features and climate sensitivity. *Clim. Past* **16**, 2095–2123 (2020).
61. Haug, G. H., Sigman, D. M., Tiedemann, R., Pedersen, T. F. & Sarnthein, M. Onset of permanent stratification in the subarctic Pacific Ocean. *Nature* **401**, 779–782 (1999).
62. Hobgood, J. S. & Cerveny, R. S. Ice-age hurricanes and tropical storms. *Nature* **333**, 243–245 (1988).
63. Yoo, J., Galewsky, J., Camargo, S. J., Korty, R. & Zamora, R. Dynamical downscaling of tropical cyclones from CCSM4 simulations of the Last Glacial Maximum. *JAMES* **8**, 1229–1247 (2016).
64. Lawton, Q. A., Korty, R. L. & Zamora, R. A. Tropical cyclones downscaled from simulations of the Last Glacial Maximum. *J. Climate* **34**, 659–674 (2021).
65. Harrison, S. P. et al. Climate model benchmarking with glacial and mid-Holocene climates. *Clim. Dyn.* **43**, 671–688 (2014).
66. Harrison, S. P. et al. Evaluations of CMIP5 palaeo-simulations to improve climate projections. *Nat. Clim. Change* **5**, 735–743 (2015).
67. Yan, Q. & Zhang, Z. Dominating roles of ice sheets and insolation in variation of tropical cyclone genesis potential over the North Atlantic during the last 21,000 years. *Geophys. Res. Lett.* **44**, 10624–10632 (2017).
68. Boos, W. R. & Korty, R. L. Regional energy budget control of the intertropical convergence zone and application to mid-Holocene rainfall. *Nat. Geosci.* **9**, 892–897 (2016).
69. Adam, O., Schneider, T., Enzel, Y. & Quade, J. Both differential and equatorial heating contributed to African monsoon variations during the mid-Holocene. *Earth Planet. Sci. Lett.* **522**, 20–29 (2019).
70. Lamy, F. et al. Precession modulation of the South Pacific westerly wind belt over the past million years. *Proc. Natl Acad. Sci. USA* **116**, 23455–23460 (2019).
71. Routson, C. et al. Mid-latitude net precipitation decreased with Arctic warming during the Holocene. *Nature* **568**, 83–87 (2019).
72. Henry, L. G. et al. North Atlantic Ocean circulation and abrupt climate change during the last glaciation. *Science* **353**, 470–474 (2016).
73. McGee, D., Moreno-Chamarro, E., Marshall, J. & Galbraith, E. D. Western US lake expansions during Heinrich stadials linked to Pacific Hadley circulation. *Sci. Adv.* **4**, eaav0118 (2018).
74. Yang, Y. et al. Latitudinal response of storm activity to abrupt climate change during the last 6,500 years. *Geophys. Res. Lett.* **47**, e2020GL089859 (2020).
75. McGee, D., Donohoe, A., Marshall, J. & Ferreira, D. Changes in ITCZ location and cross-equatorial heat transport at the Last Glacial Maximum, Heinrich Stadial 1, and the mid-Holocene. *Earth Planet. Sci. Lett.* **390**, 69–79 (2014).
76. Pausata, F. S. R. et al. Tropical cyclone activity enhanced by Sahara greening and reduced dust emissions during the African Humid Period. *Proc. Natl Acad. Sci* **114**, 6221–6226 (2017).
77. Dandoy, S. et al. Atlantic hurricane response to Saharan greening and reduced dust emissions during the mid-Holocene. *Clim. Past* **17**, 675–701 (2021).
78. Korty, R. L., Camargo, S. J. & Galewsky, J. Variations in tropical cyclone genesis factors in simulations of the Holocene epoch. *J. Climate* **25**, 8196–8211 (2012).
79. Evans, S., Dawson, E. & Ginoux, P. Linear relation between shifting ITCZ and dust hemispheric asymmetry. *Geophys. Res. Lett.* **47**, e2020GL090499 (2020).
80. Yan, Q., Korty, R. & Zhang, Z. Tropical cyclone genesis factors in a simulation of the last two millennia: results from the Community Earth System Model. *J. Climate* **28**, 7182–7202 (2015).
81. Baldini, L. M. et al. Persistent northward North Atlantic tropical cyclone track migration over the past five centuries. *Sci. Rep.* **6**, 37522 (2016).
82. Donnelly, J. P. et al. Climate forcing of unprecedented intense-hurricane activity in the last 2000 years. *Earth's Future* **3**, 49–65 (2015).
83. Mann, M. E., Woodruff, J. D., Donnelly, J. P. & Zhang, Z. Atlantic hurricanes and climate over the past 1,500 years. *Nature* **460**, 880–883 (2009).
84. Bramante, J. F. et al. Increased typhoon activity in the Pacific deep tropics driven by Little Ice Age circulation changes. *Nat. Geosci.* **13**, 806–811 (2020).
85. Rustic, G. T., Koutavas, A., Marchitto, T. M. & Linsley, B. K. Dynamical excitation of the tropical Pacific Ocean and ENSO variability by Little Ice Age cooling. *Science* **350**, 1537–1541 (2015).
86. Altman, J. et al. Poleward migration of the destructive effects of tropical cyclones during the 20th century. *Proc. Natl Acad. Sci. USA* **115**, 11543–11548 (2018).

87. Donnelly, J. P. & Woodruff, J. D. Intense hurricane activity over the past 5,000 years controlled by El Niño and the West African monsoon. *Nature* **447**, 465–468 (2007).
88. Hernandez, A. et al. Modes of climate variability: synthesis and review of proxy-based reconstructions through the Holocene. *Earth Sci. Rev.* **209**, 103286 (2020).
89. Van Hengstum, P. J. et al. The intertropical convergence zone modulates intense hurricane strikes on the western North Atlantic margin. *Sci. Rep.* **6**, 21728 (2016).
90. Liu, K.-B. & Fearn, M. L. Reconstruction of prehistoric landfall frequencies of catastrophic hurricanes in northwestern Florida from lake sediment records. *Quat. Res.* **54**, 238–245 (2000).
91. Liu, K.-B. & Fearn, M. L. Lake-sediment record of late Holocene hurricane activities from coastal Alabama. *Geology* **21**, 793–796 (1993).
92. Wallace, E. J., Coats, S., Emanuel, K. & Donnelly, J. P. Centennial-scale shifts in storm frequency captured in paleohurricane records from the Bahamas arise predominately from random variability. *Geophys. Res. Lett.* **47**, e2020GL091145 (2020).
93. Wallace, E. J. et al. Intense hurricane activity over the past 1500 years at South Andros Island, The Bahamas. *Paleooceanogr. Paleoclimatol.* **34**, 1761–1783 (2019).
94. Kossin, J. P., Emanuel, K. & Vecchi, G. A. The poleward migration of the location of tropical cyclone maximum intensity. *Nature* **509**, 349–352 (2014).
95. Daloz, A. S. & Camargo, S. J. Is the poleward migration of tropical cyclone maximum intensity associated with a poleward migration of tropical cyclone genesis? *Clim. Dyn.* **50**, 705–715 (2018).
96. Studholme, J. & Gulev, S. Concurrent changes to Hadley circulation and the meridional distribution of tropical cyclones. *J. Climate* **31**, 4367–4389 (2018).
97. Hodges, K., Cobb, A. & Vidale, P. L. How well are tropical cyclones represented in reanalysis datasets. *J. Climate* **30**, 5243–5264 (2017).
98. Wang, C., Wang, L., Wang, X., Wang, D. & Wu, L. North–South variations of tropical storm genesis locations in the Western Hemisphere. *Geophys. Res. Lett.* **43**, 11367–11374 (2016).
99. Sharmila, S. & Walsh, K. J. E. Recent poleward shift of tropical cyclone formation linked to Hadley cell expansion. *Nat. Clim. Change* **8**, 730–736 (2018).
100. Sun, Y. et al. Impact of ocean warming on tropical cyclone size and its destructiveness. *Sci. Rep.* **7**, 8154 (2017).
101. Zhan, R. & Wang, Y. Weak tropical cyclones dominate the poleward migration of the annual mean location of lifetime maximum intensity of northwest Pacific tropical cyclones since 1980. *J. Climate* **30**, 6873–6882 (2017).
102. Feng, X., Klingaman, N. P. & Hodges, K. I. Poleward migration of western North Pacific tropical cyclones related to changes in cyclone seasonality. *Nat. Commun.* **12**, 6210 (2021).
103. Mokhov, I. I., Makarova, M. E. & Poroshenko, A. G. Tropical cyclones and their transformation into extratropical: estimates of the half-century trends. *Phys. Atmos.* **493**, 592–597 (2020).
104. Kossin, J. P., Emanuel, K. & Camargo, S. J. Past and projected changes in western North Pacific tropical cyclone exposure. *J. Climate* **29**, 5725–5739 (2016).
105. Song, J. & Klotzbach, P. J. What has controlled the poleward migration of annual averaged location of tropical cyclone lifetime maximum intensity over the western North Pacific since 1961? *Geophys. Res. Lett.* **45**, 1148–1156 (2018).
106. Vecchi, G. A. & Soden, B. J. Increased tropical Atlantic wind shear in model projections of global warming. *Geophys. Res. Lett.* **34**, L08702 (2007).
107. Bell, S. S., Chand, S. S. & Turville, C. Projected changes in ENSO-driven regional tropical cyclone tracks. *Clim. Dyn.* **54**, 2533–2559 (2020).
108. Zhang, L. & Karnauskas, K. B. The role of tropical interbasin SST gradients in forcing Walker circulation trends. *J. Climate* **30**, 499–508 (2017).
109. Hu, S. & Fedorov, A. V. Cross-equatorial winds control El Niño diversity and change. *Nat. Clim. Change* **8**, 798–802 (2018).
110. Heade, U. K. & Fedorov, A, V. Eastern equatorial Pacific warming delayed by aerosols and thermostat response to CO_2 increase. *Nat. Clim. Change* **11**, 696–703 (2021).
111. Zhang, W. et al. Dominant role of Atlantic multidecadal oscillation in the recent decadal changes in western North Pacific tropical cyclone activity. *Geophys. Res. Lett.* **45**, 354–362 (2018).
112. Zhao, B. & Fedorov, A. The seesaw response of the intertropical and South Pacific convergence zones to hemispherically asymmetric thermal forcing. *Clim. Dyn.* **54**, 1639–1653 (2020).
113. Retsch, M. H., Mauritsen, T. & Hohnegger, C. Climate change feedbacks in aquaplanet experiments with explicit parameterised convection for horizontal resolutions of 2,525 up to 5 km. *J. Adv. Model. Earth Syst.* **11**, 2070–2088 (2019).
114. Merlis, T. M., Zhao, M. & Held, I. M. The sensitivity of hurricane frequency to ITCZ changes and radiatively forced warming in aquaplanet simulations. *Geophys. Res. Lett.* **40**, 4109–4114 (2013).
115. Walsh, K. J. E. et al. Real world and tropical cyclone world. Part II: sensitivity of tropical cyclone formation to uniform and meridionally varying sea surface temperatures under aquaplanet conditions. *J. Climate* **33**, 1473–1486 (2020).
116. Emanuel, K., Sundararajan, R. & Williams, J. Hurricanes and global warming: results from downscaling IPCC AR4 simulations. *Bull. Am. Meteorol. Soc.* **89**, 347–368 (2008).
117. Bell, R., Strachan, J., Vidale, P. L., Hodges, K. & Roberts, M. Response of tropical cyclones to idealized climate change experiments in a global high-resolution coupled general circulation model. *J. Climate* **26**, 7966–7980 (2013).
118. Murakami, H., Delworth, T. L., Cooke, W. F., Zhao, M. & Xiang, B. Detected climatic change in global distribution of tropical cyclones. *Proc. Natl Acad. Sci. USA* **117**, 10706–10714 (2020).
119. Bell, S. S. et al. Western North Pacific tropical cyclone tracks in CMIP5 models: statistical assessment using a model-independent detection and tracking scheme. *J. Climate* **32**, 7191–7208 (2019).
120. Bell, S. S. et al. Projections of southern hemisphere tropical cyclone track density using CMIP5 models. *Clim. Dyn.* **52**, 6065–6079 (2019).
121. Tang, B. & Camargo, S. J. Environmental control of tropical cyclones in CMIP5: a ventilation perspective. *JAMES* **6**, 115–128 (2014).
122. Li, T. et al. Global warming shifts Pacific tropical cyclone location. *Geophys. Res. Lett.* **37**, L21804 (2010).
123. Chu, J.-E. et al. Reduced tropical cyclone densities and ocean effects due to anthropogenic greenhouse warming. *Sci. Adv.* **6**, eabd5109 (2020).
124. Murakami, H., Wang, B., Li, T. & Kitoh, A. Projected increase in tropical cyclones near Hawaii. *Nat. Clim. Change* **3**, 749–754 (2013).
125. Nakamura, J. et al. Western North Pacific tropical cyclone model tracks in present and future climates. *J. Geophys. Res. Atmos.* **122**, 9721–9744 (2017).
126. Liu, M., Vecchi, G. A., Smith, J. A. & Murakami, H. The present-day simulation and twenty-first century projection of the climatology of extratropical transition in the North Atlantic. *J. Climate* **30**, 2739–2756 (2017).
127. Michaelis, A. C. & Lackmann, G. M. Climatological changes in the extratropical transition of tropical cyclones in high-resolution global simulations. *J. Climate* **32**, 8733–8753 (2019).
128. Jung, C. & Lackmann, G. M. The response of extratropical transition of tropical cyclones to climate change: quasi-idealized numerical experiments. *J. Climate* **34**, 4361–4381 (2021).
129. Zhang, G., Murakami, H., Knutson, T. R., Mizuta, R. & Yoshida, K. Tropical cyclone motion in a changing climate. *Sci. Adv.* **6**, eaaz7610 (2020).
130. Camargo, S. Global and regional aspects of tropical cyclone activity in CMIP5 models. *J. Climate* **26**, 9880–9902 (2013).
131. Wang, C., Zhang, L., Lee, S.-K., Wu, L. & Mechoso, C. R. A global perspective on CMIP5 climate model biases. *Nat. Clim. Change* **4**, 201–205 (2014).
132. Byrne, M. P., Pendergrass, A. G., Rapp, A. D. & Wodzicki, K. R. Response of the Intertropical Convergence Zone to climate change: location, width, and strength. *Curr. Clim. Change Rep.* **4**, 355–370 (2018).
133. Staten, P. W., Lu, J., Grise, K. M., Davis, S. M. & Birner, T. Re-examining tropical expansion. *Nat. Clim. Change* **8**, 768–775 (2018).
134. Shaw, T. A. Mechanisms of future predicted changes in the zonal mean mid-latitude circulation. *Curr. Clim. Change Rep.* **5**, 345–357 (2019).
135. Maher, P., Kelleher, M. E., Sansom, P. G. & Methven, J. Is the subtropical jet shifting poleward? *Clim. Dyn.* **54**, 1741–1759 (2020).
136. Salmon, R., Held, I. M., Fields, J. & Thiffeault, J.-L. *The General Circulation of the Atmosphere: 2000 Program in Geophysical Fluid Dynamics* (Woods Hole Oceanographic Institute, 2001).
137. Davis, N. & Birner, T. On the discrepancies in tropical belt expansion between reanalyses and climate models and among tropical belt width metrics. *J. Climate* **30**, 1211–1231 (2017).
138. Menzel, M. E., Waugh, D. & Grise, K. Disconnect between Hadley cell and subtropical jet variability and response to increased CO_2. *Geophys. Res. Lett.* **46**, 7045–7053 (2019).
139. Waugh, D. W. et al. Revisiting the relationship among metrics of tropical expansion. *J. Climate* **31**, 7565–7581 (2018).
140. Chemke, R. & Polvani, L. M. Exploiting the abrupt $4\times CO_2$ scenario to elucidate tropical expansion mechanisms. *J. Climate* **32**, 859–875 (2019).
141. Raghavendra, A., Roundy, P. E. & Zhou, L. Trends in tropical wave activity from the 1980s to 2016. *J. Climate* **32**, 1661–1676 (2019).
142. Emanuel, K. The behaviour of a simple hurricane model using a convective scheme based on subcloud layer entropy equilibrium. *J. Atmos. Sci.* **52**, 3960–3968 (1995).
143. Held, I. M. & Soden, B. J. Robust responses of the hydrological cycle to global warming. *J. Climate* **19**, 5686–5699 (2006).
144. Chavas, D. R. & Reed, K. A. Dynamical aquaplanet experiments with uniform thermal forcing: system dynamics and implications for tropical cyclone genesis and size. *J. Atmos. Sci.* **76**, 2257–2274 (2019).
145. Bembenek, E., Merlis, T. M. & Straub, D. N. Influence of latitude and moisture effects on the barotropic instability of an idealised ITCZ. *J. Atmos. Sci.* (in the press); https://journals.ametsoc.org/view/journals/atsc/aop/JAS-D-20-0346.1/JAS-D-20-0346.1.xml

146. Ferreira, R. N. & Schubert, W. H. Barotropic aspects of ITCZ breakdown. *J. Atmos. Sci.* **54**, 261–285 (1997).
147. Klotzbach, P. The Madden–Julian oscillation's impacts on worldwide tropical cyclone activity. *J. Climate* **27**, 2317–2330 (2014).
148. Fine, C. M., Johnson, R. H., Ciesielski, P. E. & Taft, R. K. The role of topographically induced vortices in tropical cyclone formation over the Indian Ocean. *Mon. Weather Rev* **144**, 4827–4847 (2016).
149. Rios-Berrios, R., Medeiros, B. & Bryan, G. H. Mean climate and tropical rainfall variability in aquaplanet simulations using the model for prediction across scales—atmosphere. *JAMES* **12**, e2020MS002102 (2020).
150. Sriver, R. L. & Huber, M. Observational evidence for an ocean heat pump induced by tropical cyclones. *Nature* **44**, 577–580 (2007).
151. Korty, R. L., Emanuel, K. A. & Scott, J. R. Tropical cyclone-induced upper-ocean mixing and climate: application to equable climates. *J. Clim.* **21**, 638–654 (2008).
152. Huang, A., Li, H., Sriver, R. L., Fedorov, A. V. & Brierley, C. M. Regional variations in the ocean response to tropical cyclones: ocean mixing versus low cloud suppression. *Geophys. Res. Lett.* **44**, 1947–1955 (2017).
153. O'Neill, B. C. et al. The scenario model intercomparison project (ScenarioMIP) for CMIP6. *Geosci. Model Dev.* **9**, 3461–3482 (2016).
154. *Fields from the Visible Infrared Imaging Radiometer Suite (VIRRS) aboard the Suomi National Polar-orbiting Partnership (NPP) Satellite* (EOSDIS, accessed 21 September 2021); https://worldview.earthdata.nasa.gov/
155. Bony, S. et al. Cloud, circulation, and climate sensitivity. *Nat. Geosci.* **8**, 261–268 (2015).
156. Bell, B., Hersbach, H., Berrisford, P., Dahlgren, P., Horányi, A., Muñoz Sabater, J., Nicolas, J., Radu, R., Schepers, D., Simmons, A., Soci, C., Thépaut, J-N. *ERA5 Monthly Averaged Data on Pressure Levels from 1950 to 1978 (Preliminary Version)* (Copernicus Climate Change Service (C3S) Climate Data Store (CDS, 2020); https://cds.climate.copernicus-climate.eu/cdsapp#!/dataset/reanalysis-era5-pressure-levels-monthly-means-preliminary-back-extension?tab=overview
157. Knapp, K. R., Diamond, H. J., Kossin, J. P., Kruk, M. C. & Schreck, C. J. *International Best Track Archive for Climate Stewardship (IBTrACS) Project, Version 04r00* (NOAA National Centers for Environmental Information; accessed 21 May 2021); https://www.ncdc.noaa.gov/ibtracs/index.php?name=ib-v4-access
158. Dix, M. et al. *CSIRO-ARCCSS ACCESS-CM2 Model Output Prepared for CMIP6 CMIP* (Earth System Grid Federation, 2019); https://doi.org/10.22033/ESGF/CMIP6.4271
159. Ziehn, T. et al. *CSIRO ACCESS-ESM1.5 Model Output Prepared for CMIP6 C4MIP* (Earth System Grid Federation, 2019); https://doi.org/10.22033/ESGF/CMIP6.2286
160. Zhang, F. et al. *BCC BCC-CSM2MR Model Output Prepared for CMIP6 C4MIP* (Earth System Grid Federation, 2019); https://doi.org/10.22033/ESGF/CMIP6.1723
161. Rong, X. *CAMS CAMS_CSM1.0 Model Output Prepared for CMIP6 CMIP* (Earth System Grid Federation, 2019); https://doi.org/10.22033/ESGF/CMIP6.1399
162. Danabasoglu, G. *NCAR CESM2-WACCM Model Output Prepared for CMIP6 AerChemMIP* (Earth System Grid Federation, 2019); https://doi.org/10.22033/ESGF/CMIP6.10023
163. Huang, W. *THU CIESM Model Output Prepared for CMIP6 CMIP* (Earth System Grid Federation, 2019); https://doi.org/10.22033/ESGF/CMIP6.1352
164. Swart, N. C. et al. *CCCma CanESM5 Model Output Prepared for CMIP6 C4MIP* (Earth System Grid Federation, 2019); https://doi.org/10.22033/ESGF/CMIP6.1301
165. EC-Earth Consortium (EC-Earth) *EC-Earth-Consortium EC-Earth3-Veg Model Output Prepared for CMIP6 CMIP* (Earth System Grid Federation, 2019): https://doi.org/10.22033/ESGF/CMIP6.642
166. Silvers, L. et al. *NOAA-GFDL GFDL-CM4 Model Output Prepared for CMIP6 CFMIP* (Earth System Grid Federation, 2018); https://doi.org/10.22033/ESGF/CMIP6.1641
167. Horowitz, L. W. et al. *NOAA-GFDL GFDL-ESM4 Model Output Prepared for CMIP6 AerChemMIP* (Earth System Grid Federation, 2018); https://doi.org/10.22033/ESGF/CMIP6.1404
168. Volodin, E. et al. *INM INM-CM4-8 Model Output Prepared for CMIP6 CMIP* (Earth System Grid Federation, 2019); https://doi.org/10.22033/ESGF/CMIP6.1422
169. Volodin, E. et al. *INM INM-CM5-0 Model Output Prepared for CMIP6 CMIP* (Earth System Grid Federation, 2019); https://doi.org/10.22033/ESGF/CMIP6.1423
170. Boucher, O. et al. *IPSL IPSL-CM6A-LR Model Output Prepared for CMIP6 C4MIP* (Earth System Grid Federation, 2018); https://doi.org/10.22033/ESGF/CMIP6.1521
171. Takemura, T. *MIROC MIROC6 Model Output Prepared for CMIP6 AerChemMIP* (Earth System Grid Federation, 2019); https://doi.org/10.22033/ESGF/CMIP6.9121
172. Jungclaus, J. et al. *MPI-M MPIESM1.2-HR Model Output Prepared for CMIP6 CMIP* (Earth System Grid Federation, 2019); https://doi.org/10.22033/ESGF/CMIP6.741
173. Yukimoto, S. et al. *MRI MRI-ESM2.0 Model Output Prepared for CMIP6 AerChemMIP* (Earth System Grid Federation, 2019); https://doi.org/10.22033/ESGF/CMIP6.633
174. Seland, Ø. et al. *NCC NorESM2-LM Model Output Prepared for CMIP6 CMIP* (Earth System Grid Federation, 2019); https://doi.org/10.22033/ESGF/CMIP6.502
175. Emanuel, K. An air–sea interaction theory for tropical cyclone. Part I: steady state maintenance. *J. Atmos. Sci.* **43**, 585–605 (1986).
176. Emanuel, K. The dependence of hurricane intensity on climate. *Nature* **326**, 483–485 (1987).
177. Kossin, J. P., Knapp, K. R., Olander, T. L. & Velden, C. S. Global increase in major tropical cyclone exceedance probability over the past four decades. *Proc. Ntnl Acad. Sci USA* **117**, 11975–11980 (2020).
178. Reyes, A. R. and Yang, D. Spontaneous cyclogenesis without radiative and surface flux feedbacks. *J. Atmos. Sci.* (in the press); https://journals.ametsoc.org/view/journals/atsc/aop/JAS-D-21-0098.1/JAS-D-21-0098.1.xml
179. Tang, B. & Emanuel, K. A ventilation index for tropical cyclones. *Bull. Am. Meteorol. Soc.* **12**, 1901–1912 (2012).
180. Holland, G. J. Tropical cyclone motion: environmental interaction plus a beta effect. *J. Atmos. Sci.* **40**, 328–342 (1983).
181. Smith, R. B. A hurricane beta-drift law. *J. Atmos. Sci.* **50**, 3213–3215 (1993).
182. Arakawa, A. & Schubert, W. H. Interaction of a cumulus cloud ensemble with the large-scale environment, part I. *J. Atmos. Sci.* **31**, 674–701 (1974).
183. Sobel, A. H. & Bretherton, C. S. Modeling tropical precipitation in a single column. *J. Climate* **13**, 4378–4392 (2000).
184. Emanuel, K. Inferences from simple models of slow, convective coupled processes. *J. Atmos. Sci.* **76**, 195–208 (2019).
185. Back, L. E. & Bretherton, C. S. On the relationship between SST gradients, boundary layer winds, and convergence over the tropical oceans. *J. Climate* **22**, 4182–4196 (2009).

Methods

Tropical cyclone track density. Track density is computed from the IBTrACS archive as the annual count of TC track points within 4° of each grid square (using a 0.25×0.25° grid to match the European Centre for Medium-Range Weather Forecasts (ECMWF) ERA5 fields). The temporal resolution of the underlying track data is 3 hourly. Note that North Indian Ocean tracks are masked as the TCs there began to be recorded in the dataset only in recent years.

Climate diagnostics. The climate diagnostics shown in Figs. 4 and 6 and Extended Data Fig. 7 are computed from ERA5 (ECMWF Reanalysis 5th Generation) data using the following methods.

Tropical cyclone potential intensity. PI ($m\,s^{-1}$) calculations were done for ERA5 data using Gilford's pyPI algorithm[186], an implementation of the Bister and Emanuel algorithm[187]. This method is based on the following expression:

$$\mathrm{PI}^2 = \frac{C_\mathrm{k}}{C_\mathrm{D}} \times \frac{T_\mathrm{s}}{T_\mathrm{o}} \times \left(\mathrm{CAPE}^* - \mathrm{CAPE}\right)\big|_{\mathrm{RMW}} \quad (3)$$

where C_k and C_D are the exchange coefficients for enthalpy and momentum, T_s and T_o are the temperatures (K) at the sea surface and at the TC outflow branch in the upper troposphere. CAPE* and CAPE are the convective available potential energies of the saturated air lifted from the ocean surface to the outflow level and of the boundary layer air, respectively, both evaluated at the radius of maximum winds (RMW). An alternative, more conceptually intuitive, expression for PI can be also used[188]:

$$\mathrm{PI}^2 = \underbrace{\frac{C_\mathrm{k}}{C_\mathrm{D}}}_{\text{Exchange coefficients}} \times \underbrace{\frac{(T_\mathrm{s} - T_\mathrm{o})}{T_\mathrm{o}}}_{\text{Modified Carnot efficiency}} \times \underbrace{k_\mathrm{s}^* - k}_{\text{Air—sea thermodynamic disequilibrium}}, \quad (4)$$

where k_s^* is the saturation moist enthalpy of air right at the ocean surface and k is the moist enthalpy of air in the boundary layer overlying the surface. Equation (3) is more accurate than equation (4) because the former better estimates the amount of energy available for convection[189]. PI can be then decomposed into the terms in equation (4) with equation (3) used to compute thermodynamic disequilibrium as a residual.

Genesis potential. The genesis potential (GP) is calculated using the form[190]:

$$\mathrm{GP} = |\eta|^3 \chi^{-\frac{4}{3}} \max\left[\left(\mathrm{PI} - 35\,\mathrm{ms}^{-1}\right), 0\right]^2 \left(V_\mathrm{shear} + 25\,\mathrm{ms}^{-1}\right)^{-4},$$

where η is the absolute vorticity of the flow at 850 hPa, capped at the value of $5\times10^{-5}\,s^{-1}$, PI is expressed as a flow speed, V_shear is the magnitude of wind shear estimated as the wind speed difference ($m\,s^{-1}$) between 850 and 250 hPa. χ is the moist entropy deficit in the middle troposphere defined as

$$\chi = \frac{s_\mathrm{b} - s_\mathrm{m}}{s_\mathrm{s}^* - s_\mathrm{b}},$$

where s_b, s_m and s_s^* are the moist entropies of the boundary layer and middle troposphere, and the saturation moist entropy at the sea surface, respectively. Moist entropy s is approximately defined as:

$$s = c_\mathrm{p}\ln T - R_\mathrm{d}\ln p + \frac{L_\mathrm{v} r}{T} - rR_\mathrm{v}\ln H,$$

where T and p are temperature (K) and pressure, c_p is the specific heat capacity of air at a constant pressure, L_v is the latent heat of vaporization, r is the water vapour mixing ratio, R_d and R_v are the gas constants for dry air and water vapour, respectively, and H is the relative humidity.

MSE is defined here as:

$$h = c_\mathrm{p}T + L_\mathrm{v}r + gz,$$

where g is gravitational acceleration and z is the height above the surface.

ITCZ metrics. Three metrics for the ITCZ were computed in CMIP6 data, all by standard methods (for example, Byrne et al.[132]), namely, intensity, latitude and width:

- ITCZ intensity is defined as the maximum in zonal-mean seasonal-mean precipitation.
- ITCZ latitude is defined as the latitude of the maximum in zonal-mean seasonal-mean precipitation.
- ITCZ width is defined as the cartesian distance between latitudes of zonal-mean seasonal-mean precipitation crossing the 5 mm day^{-1} threshold on either side of the ITCZ latitude.

All these metrics were computed from hemispheric zonal-mean precipitation (mm day^{-1}) and averaged over the last three decades of each CMIP6 experiment during the TC seasons for the respective hemisphere—July to October in the Northern Hemisphere and January to March in the Southern Hemisphere. These metrics are plotted in Fig. 6 and Extended Data Fig. 7 against the global maximum in zonal-mean SST (°C) during the respective TC season.

Data availability

All the data used in this study is freely and publicly available in perpetuity. The TC data for the contemporary period (Fig. 2 and Extended Data Fig. 4) are plotted directly from IBTrACS[157]. These data are freely available at https://doi.org/10.25921/82ty-9e16. Version v04r00 was downloaded and the World Meteorological Organisation's homogenization was used. Contemporary environment fields, used in Figs. 2 and 4 and in Extended Data Figs. 4, 6 and 8, were taken from ECMWF's ERA5 reanalysis product[156]. All the data were downloaded at the native horizonal resolution (0.25×0.25°) as monthly means for the years 1979 to 2020. These raw data are freely and publicly available for download at https://doi.org/10.24381/cds.6860a573. The idealized cloud-resolving modelling data is replotted from Fedorov et al.[32]. These data are freely available in the Dryad repository https://doi.org/10.5061/dryad.8pk0p2np2. The PETM modelling data (from Kiehl et al.[34]) are available at https://doi.org/10.1016/j.palaeo.2021.110421. CMIP6 data for the ITCZ plotted in Fig. 6 and Extended Data Fig. 7 were taken from 17 model centres that contributed to CMIP6. These data are available from the Earth System Grid Federation. Our CMIP6 analysis relies on subsets of the total model ensemble (+50 models). We used data from the following models: ACCESS-CM2[158], ACCESS-ESM1-5[159], BCC-CSM2-MR[160], CAMS-CSM1-0[161], CESM2-WACCM[162], CIESM[163], CanESM5[164], EC-Earth3-Veg[165], GFDL-CM4[166], GFDL-ESM4[167], INM-CM4-8[168], INM-CM5-0[169], IPSL-CM6A-LR[170], MIROC6[171], MPI-ESM1-2-HR[172], MRI-ESM2-0[173] and NorESM2-LM[174].

References

186. Gilford, D. M. pyPI (v1.3): Tropical cyclone potential intensity calculations in python. *Geosci. Model Dev.* **14**, 2351–2369 (2021).
187. Bister, M. & Emanuel, K. A. Low frequency variability of tropical cyclone potential intensity. 1. Interannual and interdecadal variability. *J. Geophys. Res. Atmos.* **107**, 4801 (2002).
188. Emanuel, K. Tropical cyclones. *Ann. Rev. Earth Planet. Sci.* **31**, 75–104 (2003).
189. Garner, S. The relationship between hurricane potential intensity and CAPE. *J. Atmos. Sci.* **72**, 141–163 (2015).
190. Emanuel, K. Tropical cyclone activity downscaled from NOAA-CIRES reanalysis, 1908–1958. *JAMES* https://agupubs.onlinelibrary.wiley.com/doi/full/10.3894/JAMES.2010.2.1 (2010).

Acknowledgements

We thank M. Byrne (at the Universities of St Andrews and Oxford) and G. Vecchi (at Princeton University) for helpful discussions. We thank C. Zarzycki (at Penn State University) for providing the PETM data and N. Henderson (at Columbia University) for assistance with CMIP6 data access. We recognize and thank NASA, NOAA, ECMWF and the CMIP6 group of the World Climate Research Programme for making their data publicly and freely available. J.S. and A.F. were supported in part by grants from NASA (80NSSC21K0558), NOAA (NA20OAR4310377) and the ARCHANGE project of the 'Make our planet great again' programme (ANR-18-MPGA-0001, the Government of the French Republic). S.G. benefited from the Russian Science Foundation grant no. 20-17-00139 and from the Agreement no. 14.W0331.0006 with the Russian Ministry of Science and Higher Education. K.E. is supported by the US National Science Foundation (ICER-1854929). K.H. acknowledges funding from the UK Natural Environment Research Council.

Author contributions

J.S. conceived the study, wrote the drafts, produced the figures and led the preparation of the manuscript with input from all the co-authors.

Competing interests

The authors declare no competing interests.

Additional information

Extended data is available for this paper at https://doi.org/10.1038/s41561-021-00859-1.

Supplementary information The online version contains supplementary material available at https://doi.org/10.1038/s41561-021-00859-1.

Correspondence should be addressed to Joshua Studholme.

Peer review information *Nature Geoscience* thanks Ryan Sriver, Joanne Muller and the other, anonymous, reviewer(s) for their contribution to the peer review of this work. Primary Handling Editor: James Super.

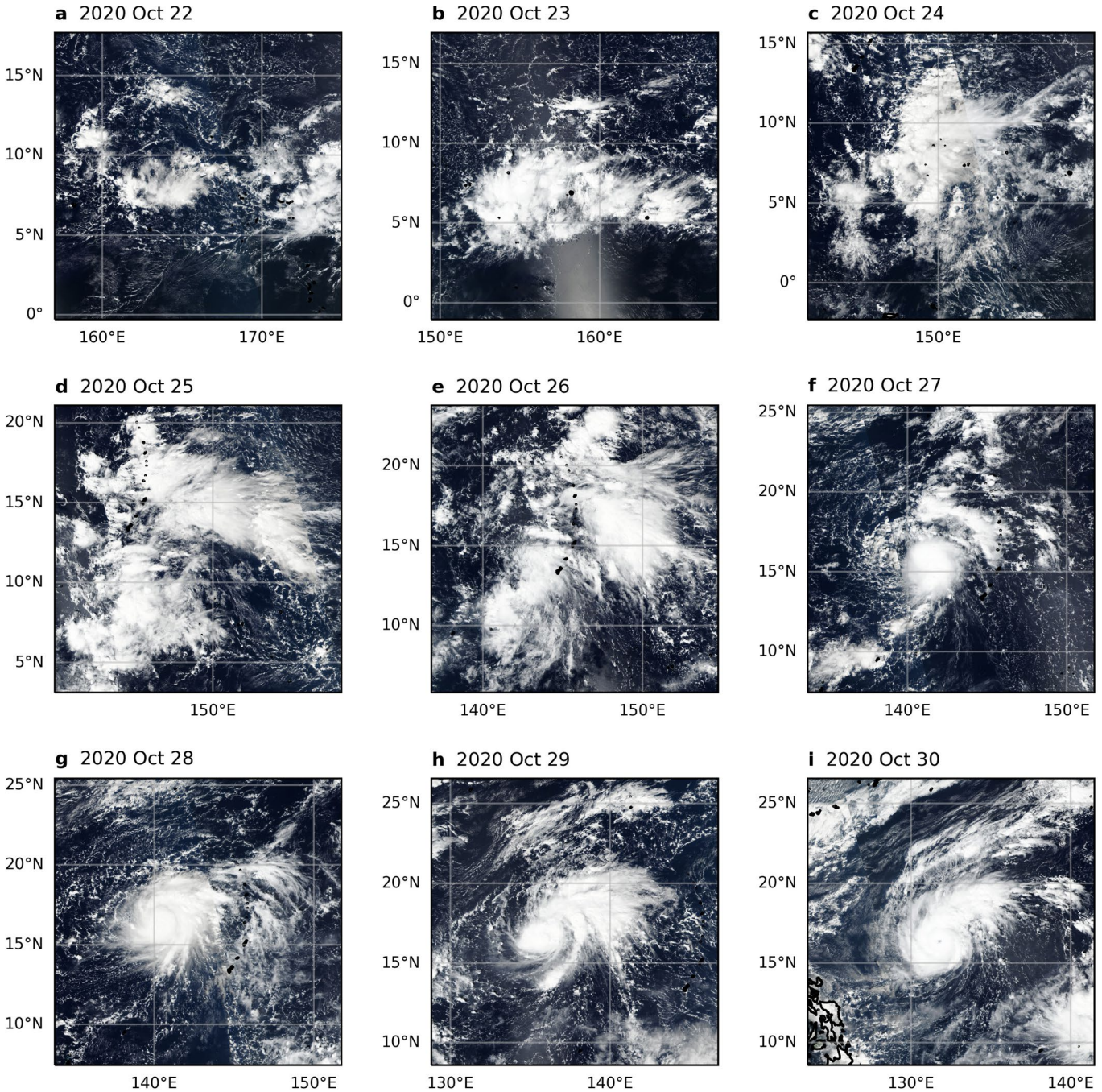

Extended Data Fig. 1 | The development and intensification of Hurricane Goni (2020, peak intensity 87 m s^{-1}). Poorly organised convection over the west Pacific warm pool aggregates over the course of three days between October 22th and 24th (**a b c**), and then acquires coherent rotation over the subsequent three days (25th to 27th, **d e f**) while propagating westward away from its seeding region. Between Oct 28th and 30th, Goni developed into a fully-fledged TC (**g h i**) and made the strongest recorded landfall event when reaching the Philippines on Oct 31st. Data from ref. [154].

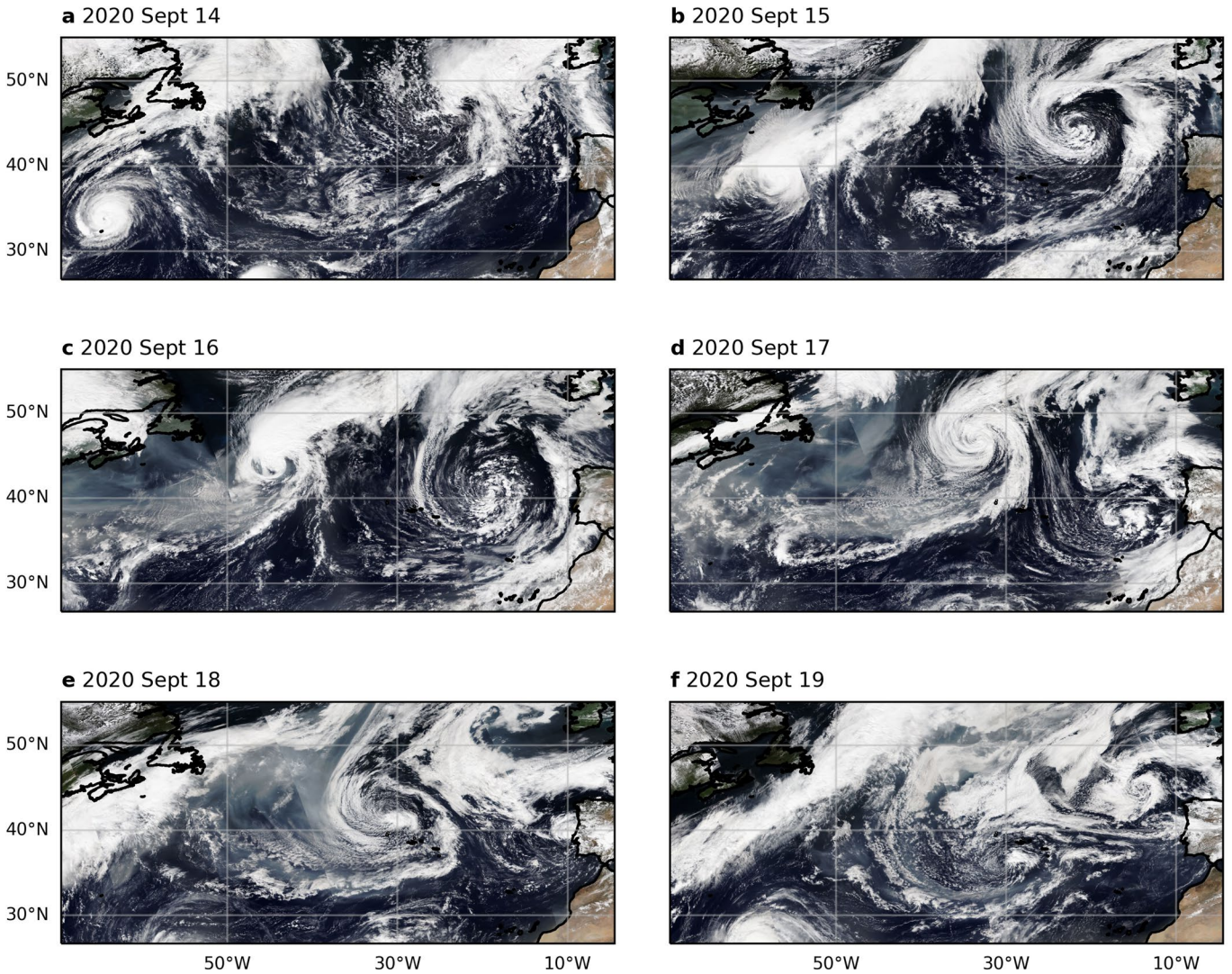

Extended Data Fig. 2 | The extratropical transition of Hurricane Paulette and the simultaneous tropical transition of Subtropical Storm Alpha. Hurricane Paulette, which originally developed out of an easterly wave on Sept 7th, reached its peak intensity on Sept 14th (47 m s^{-1}) and then underwent extratropical transition to become an extratropical cyclone on Sept 17th. It then moved south and underwent tropical transition to intensify as a tropical cyclone on Sept 22. Subtropical Storm Alpha (peak intensity 22 m s^{-1}) was the first ever tropical cyclone to make landfall in Portugal and the eastern-most genesis event in the North Atlantic record. At the same time as these events, a rare medicane developed, named Cyclone Ianos (peak intensity 34 m s^{-1}), which made landfall in Greece, seen in Extended Data Fig. 3. Data from ref. [154].

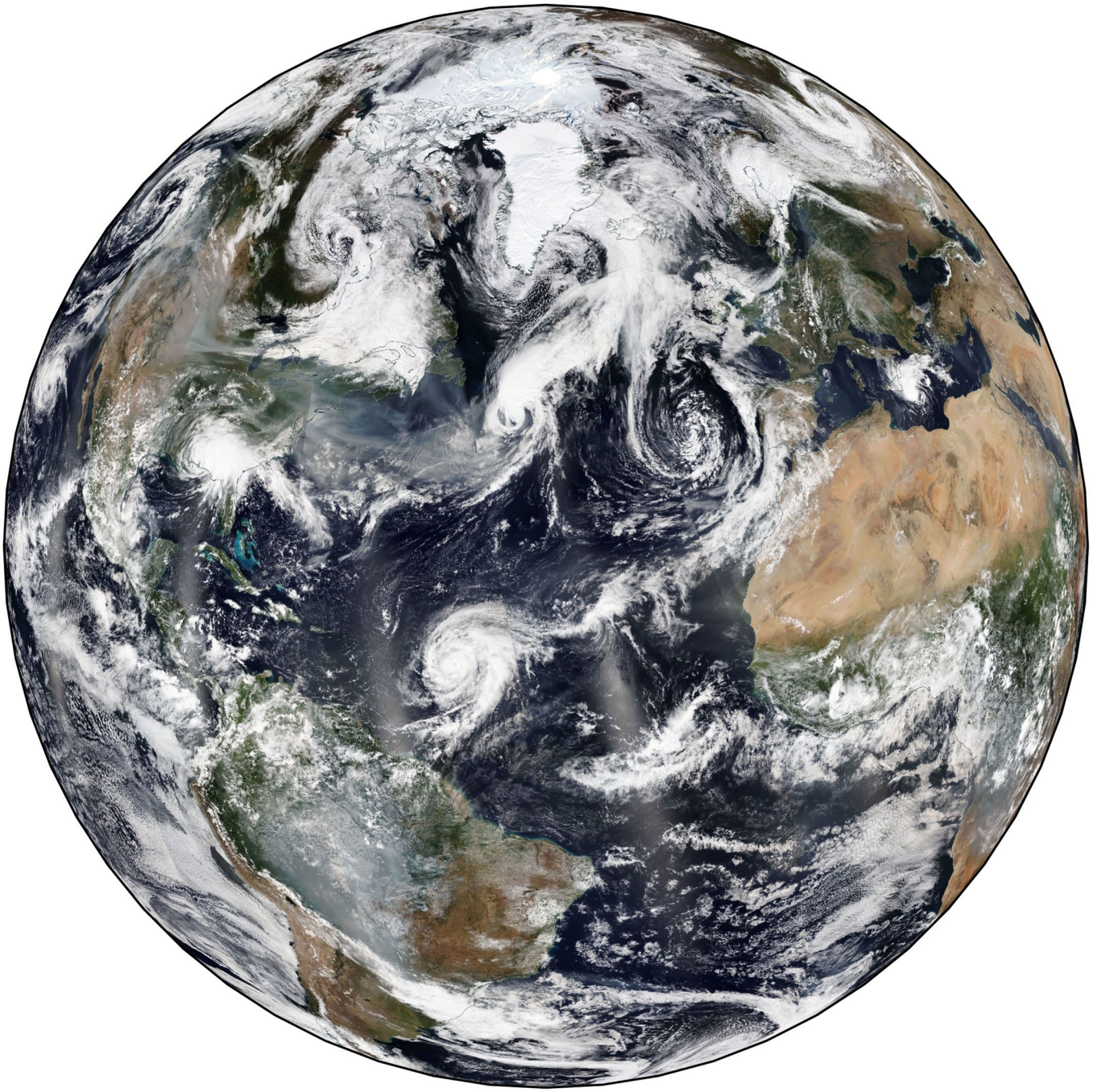

Extended Data Fig. 3 | The North Atlantic on September 16th, 2020. Hurricane Sally (peak intensity 47 m s^{-1}) can be seen making landfall over Alabama in the US, while Hurricane Teddy (peak intensity 63 m s^{-1}) was intensifying over the tropical North Atlantic and to its northeast, Tropical Storm Vicky is being weakened by strong environmental wind shear. Hurricane Paulette can be seen midway through its extratropical transition of the coast of Nova Scotia and the extratropical cutoff low that became Subtropical Storm Alpha can be seen off the coast of Portugal. In the Mediterranean, the rare Medicane Ianos can be seen south of Italy. Tropical Storms Wilfred and Beta later developed out of the organising convection visible off equatorial Africa and in the Gulf of Mexico respectively. Data from ref. [154].

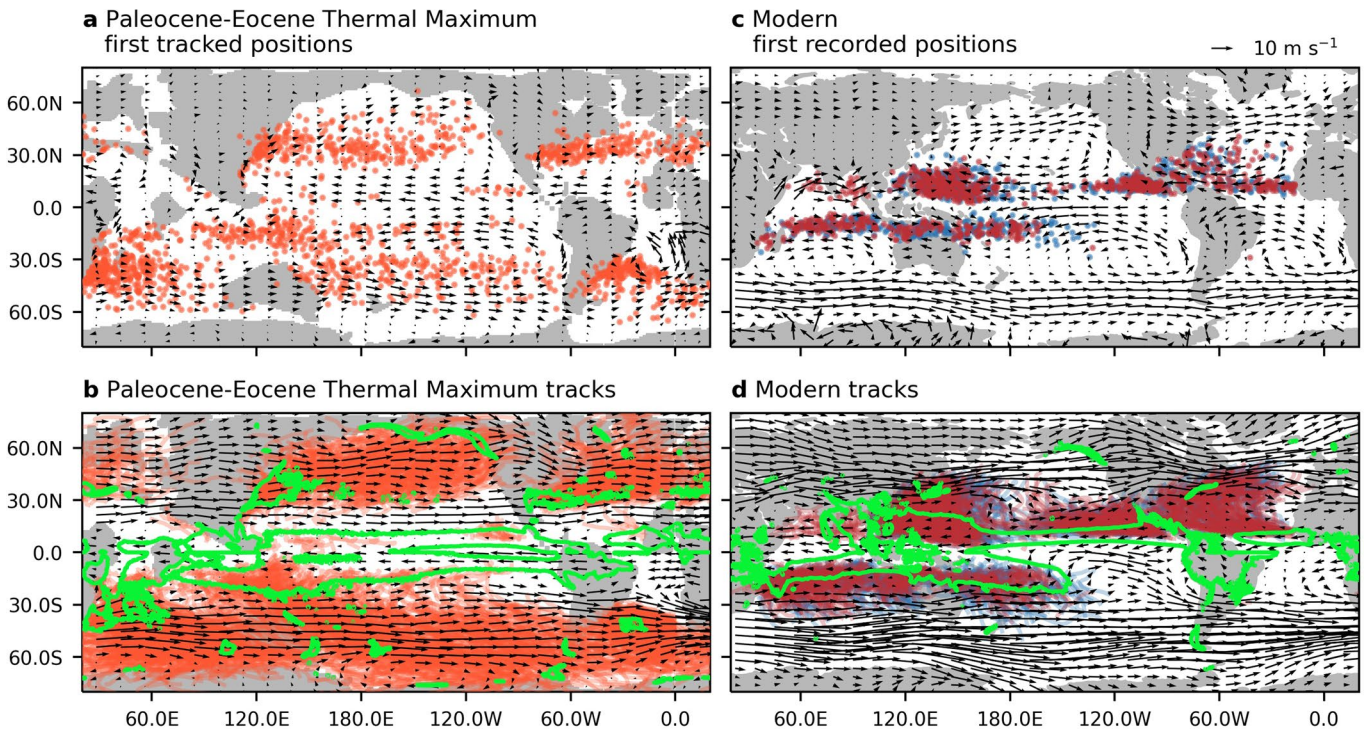

Extended Data Fig. 4 | Planetary-scale atmospheric circulation, precipitation, and TC activity during the simulated Paleocene-Eocene Thermal Maximum (PETM) and the modern period. a, c First tracked positions and **b, d** TC tracks for PETM and modern climates. The green overlay in **b** and **d** show the 6.5 mm/day climatological TC season precipitation contours. PETM data is replotted from simulations in ref. [34] and modern data is from IBTrACs (methods). Red and blue dots are as in Fig. 2, blue for 1980-1999 and red for 2000-2019. Note that the lysis definition marking the end of the tracks between the PETM tracking and modern data are not easily reconcilable. The suppression of the low latitude TCs in the PETM is related to the splitting of the summertime subtropical and eddy-driven jets (Extended Data Fig. 5 and Fig. 5).

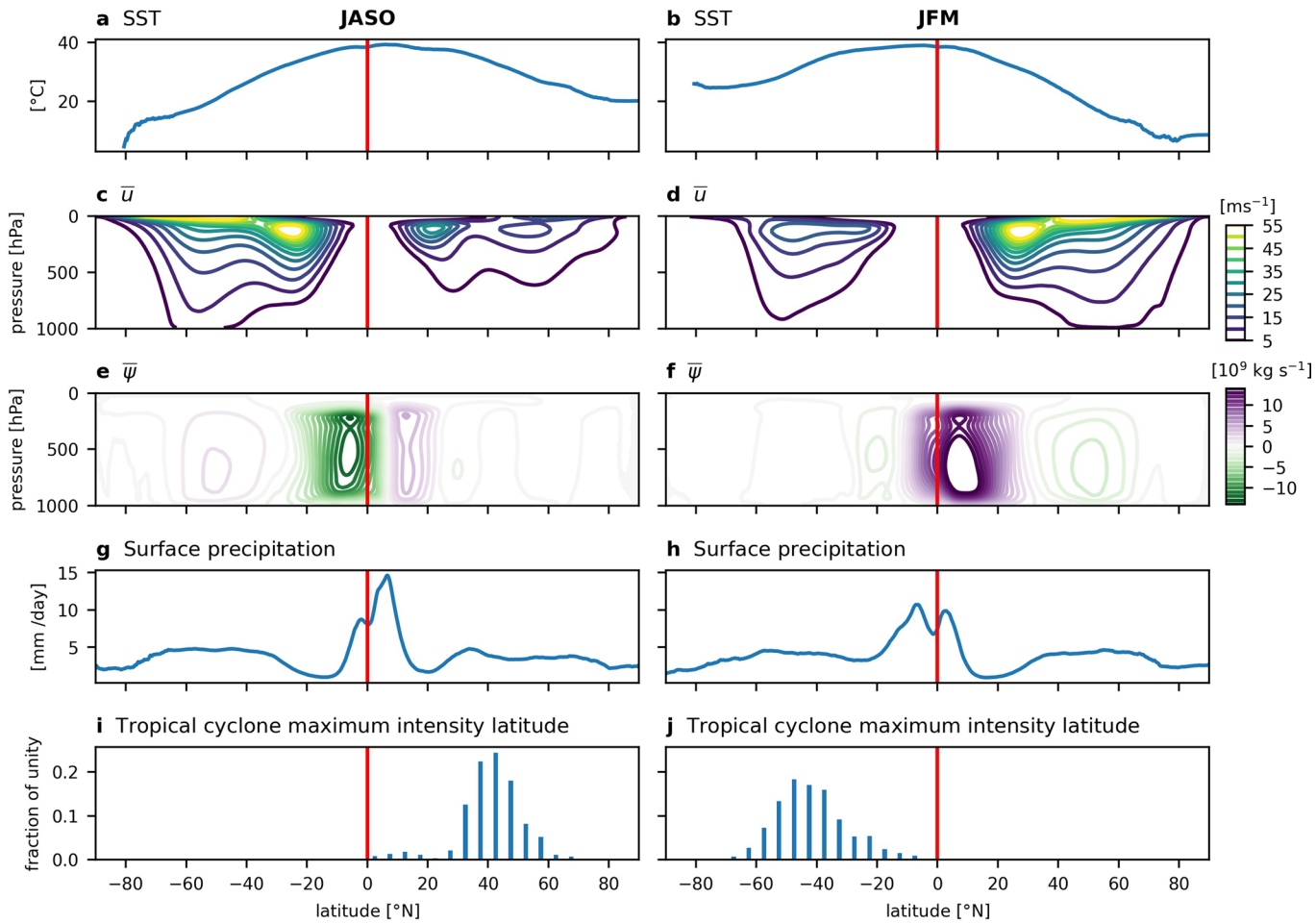

Extended Data Fig. 5 | Zonal-mean large-scale climate and north-south TC lifetime maximum intensity during the Paleocene-Eocene Thermal Maximum (PETM, CO_2 1590 ppm). Replotted from the ~0.25-degree resolution atmospheric GCM simulations of ref. [34]. Note the strong agreement on coincident jet split and TC activity in the midlatitude with the idealized cloud-system-resolving aquaplanet simulations of ref. [32] shown in Fig. 5 of the main manuscript.

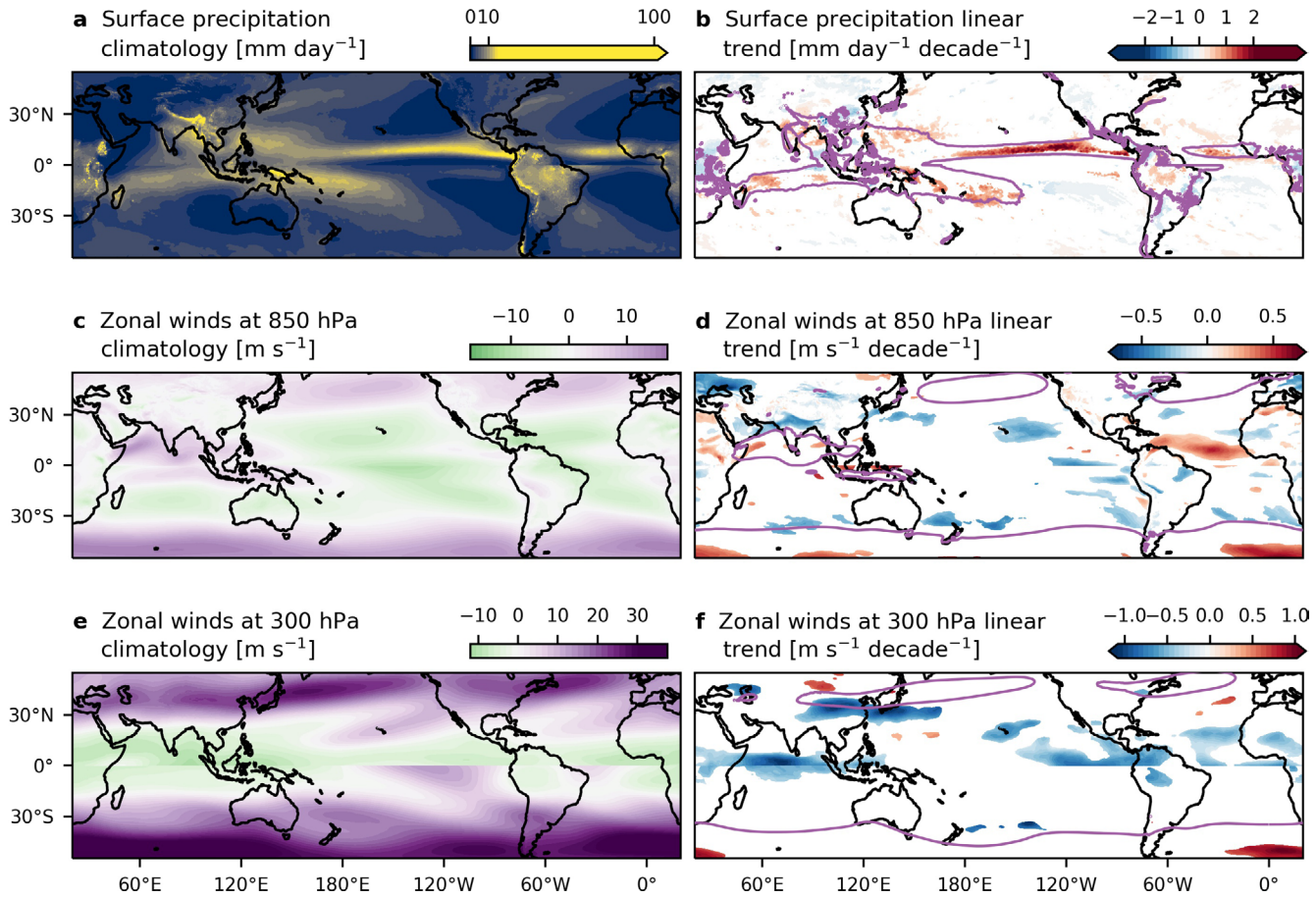

Extended Data Fig. 6 | Surface precipitation, tropospheric winds and recent linear trends from ERA5. a, **c**, **e** The 1980-2019 precipitation, and upper (300 hPa) and lower level (850 hPa) wind climatology for the tropical cyclone season (July through September for the northern hemisphere, January through March for the southern hemisphere). **b, d, f** The linear trends in these climatologies over the same period. Only trends for which *p* values are < 0.05 are plotted. The contour lines in **b**, **d**, and **f** are used to visualise the ITCZ (6.5 mm day^{-1}), and the jet stream locations (5 m s^{-1} in the lower troposphere in **d** and 20 m s^{-1} in the upper troposphere in **f**). Data from ERA5[156].

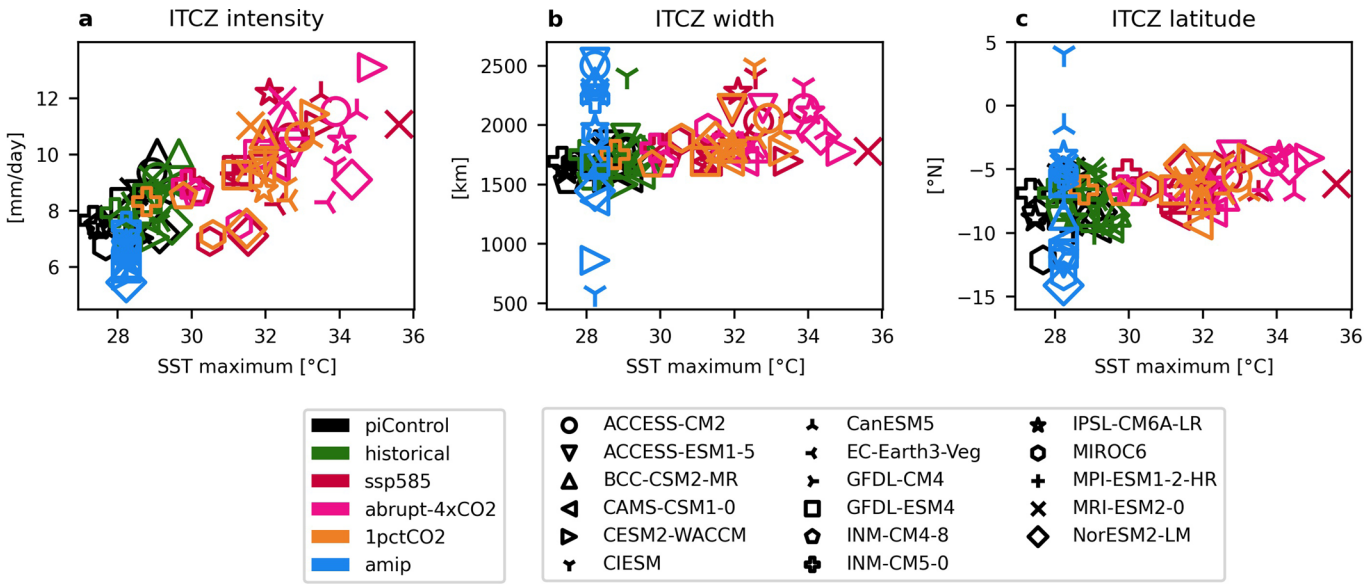

Extended Data Fig. 7 | As in Fig. 6 but for the Southern Hemisphere during TC season there: January-February-March. Note the wide range in projections for the atmosphere only ('amip') simulations in blue, highlighting the important role of atmosphere-ocean coupling in tropical climate. The largest contribution to this 'southern ITCZ' comes from the South Pacific Convergence Zone (SPCZ). Also note that these results may be affected by the models' double-ITCZ problem, which exaggerates the magnitude of the tropical convection to the south of the equator. Data from refs. [158–174].

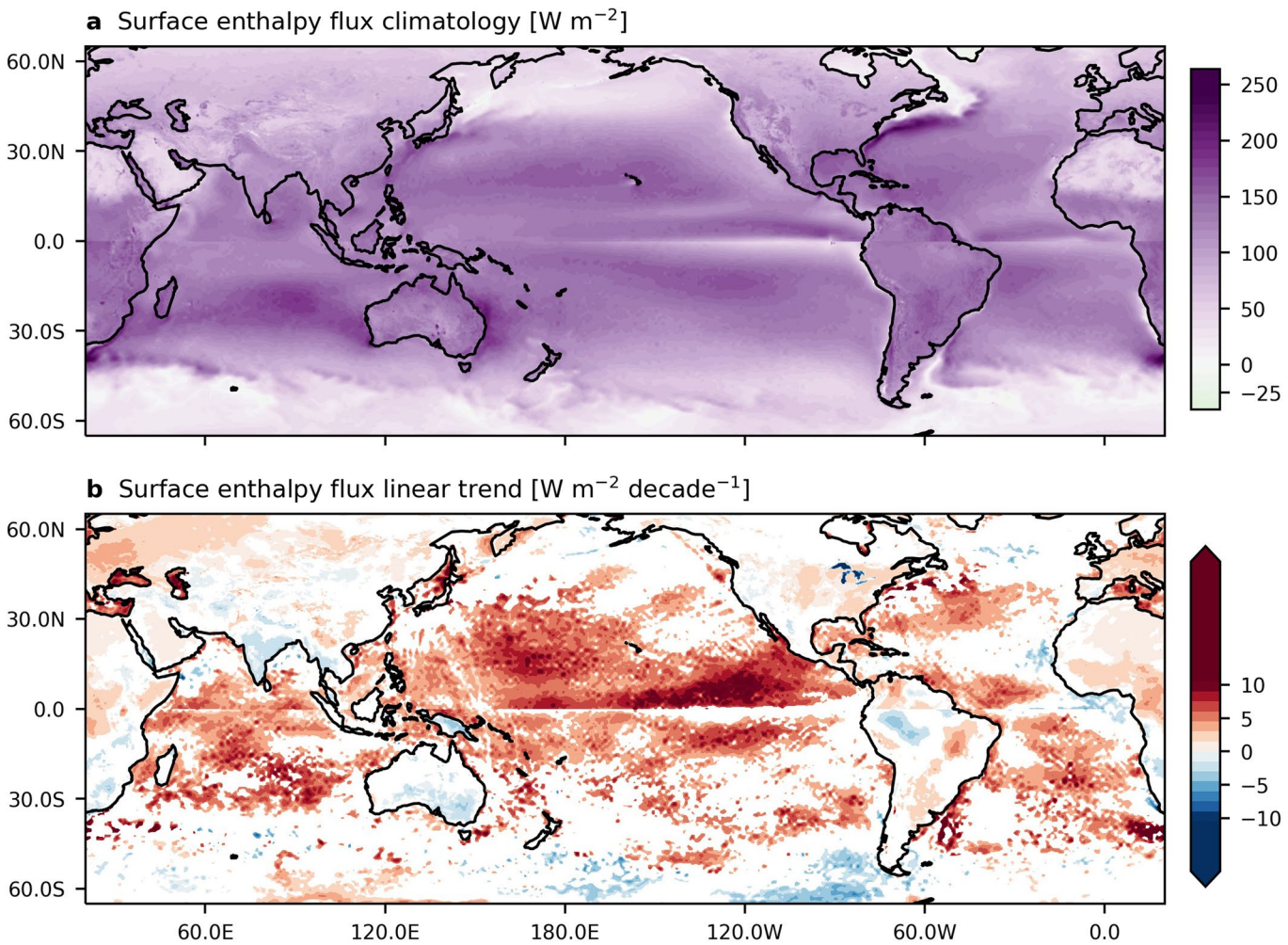

Extended Data Fig. 8 | Surface enthalpy fluxes and recent linear trends from ERA5 (1980-2019). Plotted as in Extended Data Fig. 6. Climatology and trends are for the tropical cyclone season (July through September for the northern hemisphere, January through March for the southern hemisphere). Data from ERA5[156].